UNIVERSITÀ DEGLI STUDI DI PADOVA

DIPARTIMENTO DI INGEGNERIA DELL'INFORMAZIONE

UNIVERSITÀ DEGLI STUDI DI PADOVA

Dipartimento di Ingegneria dell'Informazione

Corso di Laurea Magistrale in Bioingegneria

Particle transport and deposition analysis in diseased and stented upper airways: a parametric study

Relatrice:

Prof.ssa Francesca Maria Susin

Laureanda:

Alice Mittino

Matricola n. 1236535

Anno accademico 2021/2022

18 ottobre 2022

A thesis conducted in collaboration with

Universidad Publica de Navarra

Departamento de Ingeniería

Director:
Prof. Mauro Malvè

Abstract

The aim of the present work is the evaluation of particle transport and deposition under different conditions of the airway model. Since chronic obstructive pulmonary disease is the third leading cause of death worldwide, it is clear that studying airflow and particles dynamics in pre- and post-operatory conditions is quite important for health-risk assessment and improving drug aerosol therapies. Particular attention has been given to stenotic and stented models because there are few studies in literature under realistic breathing conditions. The model used in this study is an idealized structure that comprehend an oral tract followed by the larynx with a restricted section to simulate the glottis, and a tracheobronchial tree with asymmetric branching of straight tubes. Stenotic trachea has been designed reducing the diameter of 20%, 30% and 50% of the original healthy size. The stents used in this analysis are the Dumon stent and the Y tracheobronchial stent, with different thickness. The healthy, stenotic and stented models have been analysed under normal and forced breathing conditions for different micro-particle sizes using computational fluid dynamics. It has been found that deposition is enhanced on the bifurcation after the stenosis, for all particle diameters and degree of the stenosis. Moreover, re-adjustment of the flow at the central line makes the airflow enter the less-deviated right branch. Local overdoses is present on the stents, in percentage around 3 to 13%, increasing with the device thickness, particle size and flow rate. The aim of this work is to contribute to the understanding of particle transport and deposition in patients with airways diseases and that underwent surgery in order to improve their quality of life with proper therapies.

Sommario

L'obiettivo del presente studio è la valutazione del trasporto e della deposizione di particelle in differenti condizioni del modello delle vie aeree. Poichè la broncopneumopatia cronica ostruttiva è la terza causa di morte al mondo, è chiaro che studiare il flusso d'aria e la dinamica delle particelle in condizioni pre e post operatorie è importante per la valutazione dei rischi per la salute e per il miglioramento delle aerosolterapie. Attenzione particolare è stata data ai modelli con stenosi e stent perchè esistono pochi studi in letteratura di questi casi in condizioni respiratorie realistiche. Il modello usato in questo studio è una struttura idealizzata che comprende il tratto orale, seguito dalla laringe con una sezione ristretta che simula la glottide, e l'albero tracheobronchiale formato da tubi lineari con biforcazioni asimmetriche. La stenosi della trachea è stata riprodotta riducendo il diametro del 20%, 30% e 50% rispetto alla sua misura nel caso del modello sano. Gli stent utilizzati in questa analisi sono quello di Dumon e quello per la biforcazione tracheobronchiale, entrambi con differenti spessori. I tre modelli, sano, stenotico e con stent, sono stati analizzati in condizioni di respirazione normale e forzata con micro-particelle di varie dimensioni utilizzando la fluidodinamica computazionale. È stato trovato una maggior deposizione sulla biforcazione successiva alla stenosi, per tutte le dimensioni di particelle e gradi di stenosi. Inoltre, il riadattamento del flusso verso l'asse centrale spinge l'aria a entrare nella biforcazione destra, meno deviata. Sovradosaggi locali posso essere rilevati sugli stent, in percentuali da 3 a 13%, che aumentano con lo spessore del dispositivo, la dimensione delle particelle e la portata. Lo scopo di questo lavoro è quindi di contribuire alla comprensione del trasporto e deposizione di particelle con patologie delle vie aeree e che si sottopongono a interventi chirurgici in modo da migliorare la loro qualità di vita con terapie adeguate.

Contents

Chapter 1

Introduction

Modelling of the airflow and particle transport in human airways is essential to understand inhaled toxic material deposition as well as optimal aerosol-drug delivery to combat lung and systemic diseases. Epidemiologic studies [31, 33] have provided evidences of a correlation between particulate air pollution exposure and lung cancer and obstructive pulmonary diseases. Therefore particle transport and deposition investigations are important to discover pathophysiological mechanisms for the above diseases and to treat them in an effective way. In fact, aerosol drug therapy is a promising method of administering drugs.

Micro-particle depositions for dosimetry-and-health-risk assessment have been largely studied, but clearly simulated particles are neutral with respect to toxicity or therapeutic effect.

Computational fluid dynamics (CFD) simulations are a useful tool to characterize fluid flow and particle transport and deposition in the human airways, reducing cost and time of experiments and allowing repetitive measures that, for *in vivo* experiments, are invasive for the patient. The results of CFD have been validated by both *in vitro* experiments [13, 24, 28] and *in vivo* SPECT/CT images [13]. Due to the complexity of the human respiratory system, it is a challenging task and clearly it is not possible yet to simulate the fluid dynamics and biomechanics phenomena that occurs in a complete realistic pulmonary model.

Geometrical models are widely used to study airflow and particle transport in different conditions. The most simple and used one is Weibel's model: it assumes that each lung generation branches symmetrically into two daughter branches. Even if it is not realistic and it has been proven [29, 34] that realistic geometris predict more accurately particle deposition and transport, Weibel's models are still used to give a first insight on the matter.

Comer *et al.* first studied air flow fields in G3-G5 Weibel's model and then simulated par-

ticle transport and deposition in sequentially bifurcating airways, achieving good agreement with experimental results [10, 11]. Chen *et al.* [5] used G11-G14 Weibel's model to study particle deposition due to inertial impaction and gravitational sedimentation discovering that in deep airways for low flow rates the dominant deposition mechanism is gravitational sedimentation. As a consequence breath-holding and slow inhalation should be adopted for drug aerosol therapy in lower lung regions.

Since Weibel's model is an idealized representation of healthy adult lungs, some adaptations need to be done to simulate pathological conditions. For example Chen *et al.* studied the airflow in an obstructed pulmonary airway shrinking one of the branches to half of its original diameter to simulate a stenosis. They discovered a higher deposition efficiency of the bifurcation after the stenosis with respect to the healthy model [6]. Also Luo *et al.* [25] investigated the particle deposition in obstructed airways with stenosis at different levels of the Weibel's tree, showing that particles tend to enter the unobstructed branch or deposito on the inflammated area. The effects of the presence of a tumor on airway walls was studied by Farkas *et al.* [15] simulating the tumors with spheres of different diameters. They considered two types of tumor: sidewall and carinal tumors. The former affects both micro- and nano-particle deposition, the latter mainly large particle deposition. Farkhadnia *et al.* [16] investigated the fluid and particle dynamics in chronic bronchitis using a Weibel's G3-G6 model with complete blockage at different branching levels, coming to the conclusion that deposition mainly occurs on tubular surfaces of blocked airways because of gravitational sedimentation. Segal *et al.* [38] developed a model to compute particle deposition in chronic bronchitis and emphysema affected airways. Their findings confirm that obstructions are the main cause for deposition in chronic obstructive pulmonary diseases (COPD).

As already stated, realistic airway models describe better air flow dynamics and particle deposition. Thanks to medical imaging and with a proper geometry-file conversion, it is possible to investigate patient-specific airways segments of interest. Rahimi-Gorji *et al.* studied the airflow behavior and particle transport in healthy airways, considering first just the tracheobronchial tree down to the second bronchial bifurcation [35], and then extending the model to some more lobes and up to the oral cavity [34]. Malvè *et al.* used the computerized tomography and a file-converting software to create a CT-based model of the tracheobronchial airway to validate an impedance-based method for investigating airflow in stenotic trachea and assess the need for surgery [26]. They also compared CT-based models of patient that underwent prosthesis implantation with stented Weibel-based to understand particle transport and deposition in order to improve aerosol drug delivery therapies and their way of life [27]. Bos *et al.* [2] use CFD to study the antibiotic particle deposition in airways of patients with cystic fibrosis. They found that deposition

factors were higher in lower lobes, more diseased lobes get less drug and the deposition is highly dependent on patient-related factors. Moreover Zhang *et al.* [45] investigated particle deposition in patient with Tracheal Bronchus and COPD, which appears to occur mainly on the abnormal areas.

A trade off between realistic CT-based models and idealized Weibel models are the ones with the oral airway model proposed by Zhang *et al.* [47] that take into consideration the effects of soft palate and glottis on the airflow. They used oral model in addition with a triple symmetric bifurcation model to compare micro- and nano-particle deposition [48]. They found "hot spots" of deposition in carinal ridges for both sizes of particles, but also a more uniform deposition of nano-particles along the branches that implies greater toxicity [48]. Moreover nano-particles and small micro-particles ($d_p < 3\mu m$) reach easily deeper lung regions [22]. Brouns *et al.* [3] presented a numerical model of healthy trachea in which different stages of stenosis where imposed, in order to understand how different degrees of stenosis affect local pressure drop and the breathing. Huang *et al.* developed a human upper respiratory tract (URT) model composed by an oral section (mouth, pharynx, larynx) that take into consideration the effect of soft palate and glottis on airflow, and a tracheobronchial section with three lobes on the right side and two on the left. This model has been used to evaluate micro-particle deposition under steady inhalation [20] and transient breathing cycle [21].

The aim of the present work is to investigate airflow and micro-particle transport and deposition in an idealized upper airway model with different degrees of stenosis and after prosthetic devices implantation. Since morbidity of COPD is estimated around 10 % in adults and will increase in the next decade, it is important to evaluate the effects of obstructions on the airflow and particle deposition. Local obstructions can be solved by stents but they modify the inner lumen and, as a consequence, the airflow. Moreover, even using the most bioinert material, implantation of a prosthetic device causes inflammations and other reactions from tissues. In this perspective, studying particle deposition could enhance aerosol drug therapies to treat these symptoms and improve the quality of life of patients that undergo surgical operations.

Chapter 2

Biological and medical background

2.1 Human airways

The respiratory system is the system that takes up oxygen and expels carbon dioxide. Flow of air is driven by small pressure gradients through conducting pipes that connect the outside with the gas-exchange surface of the lungs.
The human airways can be separated in two parts depending on the location (upper and lower airways) with respect to the thoracic cage, or on their function: conducting zone and respiratory zone (where the gas-exchange takes place).
The upper airways consist of the nose and the sinuses, the oral cavity, the pharynx and the larynx. The nose and nasal cavities are divided in two halves by the nasal septum, they are covered by mucosa with ciliated and mucus-secreting cells which aim is to filter, warm and humidify the air. The larynx is separated from the pharynx by the epiglottis which control swallowing and prevent food from entering the trachea. The larynx is characterized by the glottis, a sagittal slit formed by the vocal chords that make the air vibrates and produces sounds.
The lower airways includes the extrathoracic and intrathoracic parts of the trachea, the extrapulmonary and intrapulmonary stem bronchi, the bronchioles, the alveolar ducts and alveoli. In this section the airways change from conductive to respiratory zones: at bronchioles levels start to appear alveoli where the gas-exchange takes place.
The trachea is a tube 10 to 12 cm long with a diameter of about 2 cm, stiffened by 15-20 incomplete cartilage rings. The dorsal wall of the trachea contains layer of smooth muscle that can reduce the inner lumen and shorten the length of the tube to increase or reduce resistance to the airflow.

At the carinal ridge the trachea bifurcates in the two main bronchi: the right one than branches in three lobes and the left one, more deviated, into two lobes. At this level the cartilagineous rings are more deformable; the last structures of the conducting zone

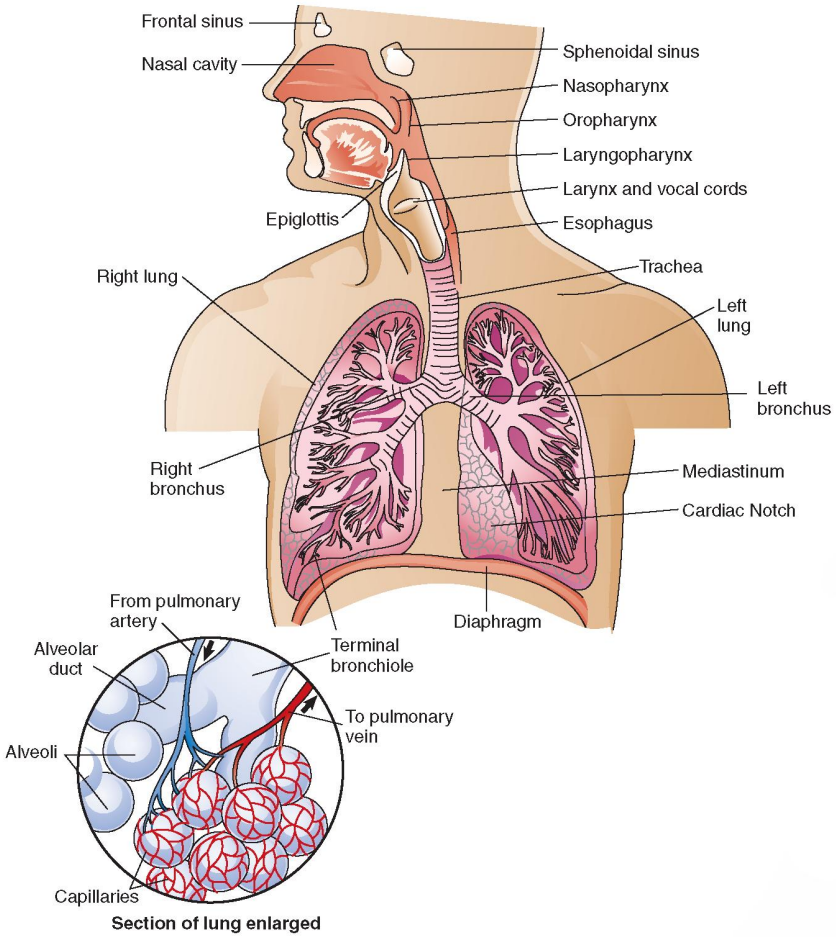

Figure 2.1: *Schematic representation of human respiratory system.*

are the bronchioles, where the lack of cartilage makes the epitelium stick to a smooth muscle layer. Irregular dichotomous branching of the airways leads to an increase of airways paths in parallel; the augmented cross-sectional diameter of airspace allows the gases to diffuse through the 140 square meters of internal surface are of the pulmonary parenchyma, the $1\mu m$-thin barrier around the alveolar sacs.

Lungs are surrounded by the visceral pleura, while the thoracic cavity is covered with the parietal pleura. These two serous membranes are separated by a thin fluid-filled space that allows the lungs to move smoothly along the thoracic wall during breathing.

The diaphragm and the intercostal muscles of the chest expand and contract the internal space of the thorax in order to generate a pressure gradient: if the pressure between the pleurae is below the atmospheric pressure the air flow inside the lung, otherwise expiration takes place.

2.1.1 Weibel's model

Weibel's lung model was designed by the biologist Ewald R. Weibel in 1963 [42] after examining and measuring adult airways from cadavers. It is the simplest but widely used airways model and consist in subsequently symmetrical bifurcating ducts, with branching angle of 35^o.

Every level of the tracheobronchial tree is called "generation" and has the same geometrical parameters. The model is divided into three main zones: the conducting airways, characterized by high flow, a transitional zone and the true respiratory zone, with low flow and high residence time.

The conducting zone consist of the tranchea (generation G0) and upper bronchial (generations G1 to G16) with smooth walls. Alveoli start to appear from G17 and their number start to increase steadily in the transitional zone. The last generations (G20 to G23) with alveolar ducts and sacs represent the true respiratory zone.

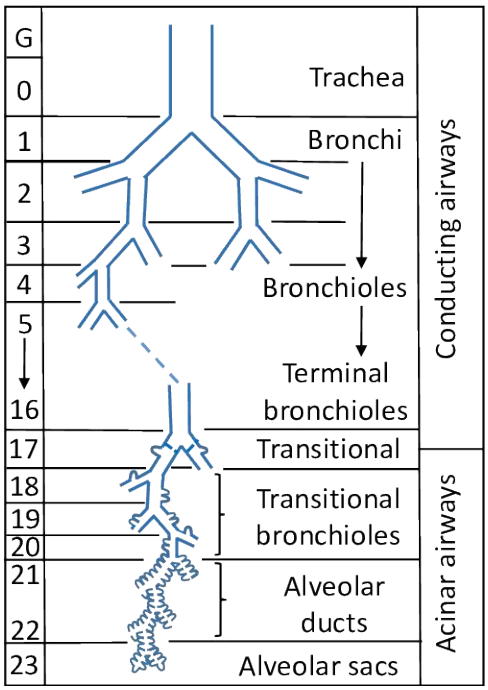

Figure 2.2: *Schematic representation of Weibel's lung model.*

2.2 COPD

Chronic Obstructive Pulmonary Disease is a common, preventable and treatable chronic lung disease that usually becomes clinically apparent at the age of 40-50 years. It is usually smoking-related, mainly in an active way but also with passive exposure to second-hand smoke, but there are a lot of other risk factors that contribute to the development of the disease. Prematurity and maternal smoking can result in poor lungs growing in utero and increased mucus secretion. Asthma and severe respiratory infections during childhood can affect the correct development of the airways and the immunological response to allergens. Other risk factors are related to exposure to indoor and outdoor air pollution due to biomass fuels and coal smoke, dusts and chemical. Dietary factors and genetic conditions need also to be considered in the health-risk assessment, indeed a deficit of alpha-1 antitrypsin, a glycoprotein that protects the alveolar walls, can cause COPD at young age. Common symptoms of COPD are breathlessness, chronic cough with phlegm and tiredness. These symptoms are often shared with asthma and people may suffer of both conditions. COPD is caused by abnormal response of the immune

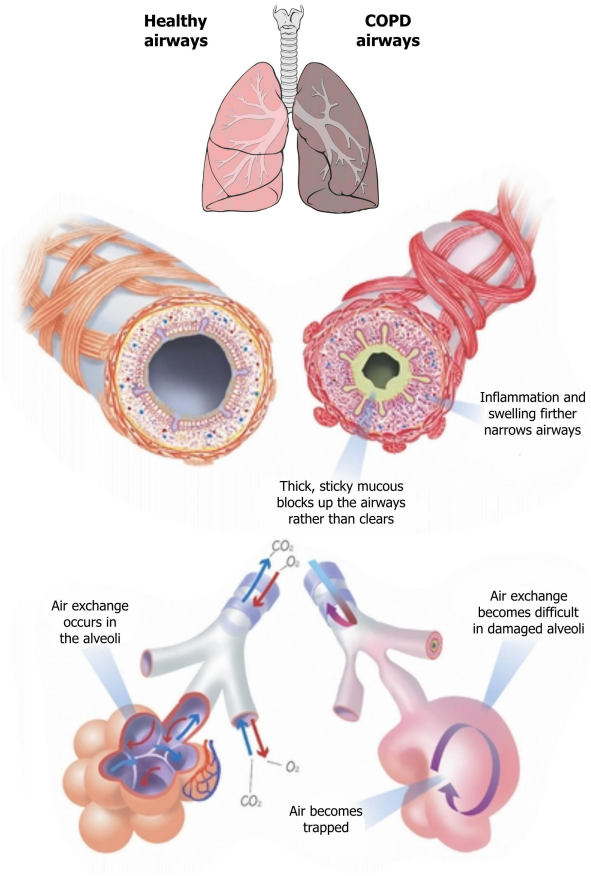

Figure 2.3: *Comparison between normal (on the left) and diseased (on the right) airways: chronic bronchitis and emphysema are typical expressions of COPD.*

system to the inhalation of toxic particles and gases. Prolonged exposure to toxic particulate can provoke chronic inflammation that is linked to tissue-remodeling. This process produces lung lesions associated with chronic bronchitis, emphysema and small-airway obstructions.

Emphysema is defined as "abnormal permanent enlargement of air spaces distal to terminal bronchioles, accompanied by destruction of their walls without obvious fibrosis" [39]. This prevent the gas-exchange to take place and is strictly linked to small-airway obstructions. Chronic bronchitis is characterised by cough and phlegm for long periods of time. It is present in smokers and patients with COPD with severe airflow obstruction. In association with respiratory infection and inflammation it contributes to more frequent chronic obstructive pulmonary disease acute exacerbations.

COPD is diagnosed through spirometry test evaluating the ratio between the forced expiratory volume in 1s and the forced vital capacity; this test reflect mainly obstruction at large airways level. Early diagnosis and treatment can slow the progression of the disease. Inhaled medications can be prescribed to improve symptoms or can be used to reduce flare-ups and are coupled with antibiotics in case of infections.

2.3 Stent

Stents are used in the respiratory system to maintain the patency of the airways in case of obstructions when there is no other surgical option. Obstructions are usually originated from inflammation, abnormal growth of tissue (as in the case of tumors, or exaggerate mucus production. The implant of this device can keep the airway lumen opened, but it may arise inflammation and cause mucosal injury.
The ideal stent should be stable, biocompatible, strong enough to resist the pressure of external forces that comprise the airways and flexible to adapt to the airways morphology during breathing, resistant to migration, available in different sizes and easily deployed and removed. In order to obtain the best features with respect to the application of the stent, different materials have been used such as silicone, nitinol and stainless steel, sometimes in combination to obtain hybrid stents.
Silicone stents are firm, stable at high temperatures and almost bioinert. They can be reinforced with polypropylene, polyamide and carbon fiber fibers which confer greater mechanical strength and resistance to the silicone matrix. Silicone stents come in various lengths, shapes, diameters and durometers. Y-shaped stents are useful to maintain patency at the main carina, in cases of bilateral bronchial involvement, or to prevent migration of a distal tracheal stent. Silicone stents can be easily customized by cutting a portion, repositioned and removed. On the other hand migration rate is quite high.

Figure 2.4: *Silicon stents produced by Novatech ©.*

Metallic stents are made from alloys. The most populars are stainless steel (old generation of stents) and nitinol (titanium and nickel alloys), a super-elastic biomaterial. Nitinol-made stents have "shape memory" that decreases risk of airway perforation, because they do not change in length once expanded, and are flexible enough to change in shape with

cough. Nowaday they are mostly repurposed for use in other organs such as the colon, esophagus, biliary tree or in the vascular system.

Figure 2.5: *Covered (A) and uncovered (B) metallic stents, taken from [43].*

They may be self-expandable or fixed-diameter stents that require balloon dilatation. They can be easily deployed via flexible bronchoscopy, but removal can result in serious complications such as tissue perforation or because tissue can grow through the mesh orifices. Metallic stents present a lot of advantages: little thickness resulting in a larger airway lumen, low migration rate and they are radio-opaque, so easy to spot on radiographic films. Moreover uncovered stents do not create obstruction across bronchial lobar orifices and, in theory, do not interrupt the mucociliary clearance. Covered metallic stents, or "hybrid stents", have been created in order to incorporate the benefit of metal and silicone stents and minimize the drawbacks of both materials. Covered metallic stents have the advantage of minimal tissue ingrowth and easier manipulation. As the covering material silicone, polyurethane and polytetrafluoroethylene (PTFE) have been used.

In the last 5 years with the developing of 3D-printing, attempts to create bioabsorbable stents have been made [14, 18] with the idea of create temporary stents that do not need additional surgery for removal. These are still prototypes, and their long-term success and complication rates are uncertain but this is a promising field as newer medical-grade materials become available.

Chapter 3

Theoretical framework

In this chapter the main physical topics are presented in order to give a complete overview and understanding of the matter.

3.1 Navier-Stokes equations

The Navier-Stokes equations are a system of six partial differential equations, one for mass conservation, three for momentum conservation and one for energy conservation. Considering the Eulerian point of view:

$$\frac{\partial \rho}{\partial t} + \nabla \cdot (\rho \, \mathbf{U}) = 0 \tag{3.1}$$

$$\frac{\partial \rho \mathbf{U}}{\partial t} + \nabla \cdot (\rho \, \mathbf{U} \otimes \mathbf{U}) = -\nabla \, p + \nabla \cdot \tau + \rho \mathbf{f} \tag{3.2}$$

$$\frac{\partial E_T}{\partial t} + \nabla \cdot (E_T \, \mathbf{U}) = -\nabla \cdot (p \, \mathbf{U}) - (\nabla \cdot q) + \left(\nabla^2 (\mathbf{U} \cdot \tau)\right) + \rho(\mathbf{f} \cdot \mathbf{U} + Q) \tag{3.3}$$

where $\mathbf{U}$ is the fluid velocity, p is the fluid pressure, ρ is the fluid density, $\mathbf{f}$ represents the external forces. τ is the stress tensor and it is given by:

$$\tau = \mu \left(\nabla \mathbf{U} + (\nabla \mathbf{U})^T - \frac{2}{3} \delta \, \nabla \cdot \mathbf{U} \right) \tag{3.4}$$

with μ fluid viscosity. In the energy conservation equation Q and q are the heat and heat flux respectively, and the total energy is given by:

$$E_T = \rho \Big(e + \frac{1}{2} \mathbf{U}^2 \Big) \tag{3.5}$$

where e is the enthalpy.
As regards the momentum conservation equation, the left side of the equivalence represent

the contribution of inertial forces, while on the right side the contribution of pressure, viscous and external forces are listed.
Analytical solution of this set of equation is still an unsolved problem of modern mathematics, currently there exist only for few simplified cases. Approximate solutions can be obtained with numerical methods and the use of computers.

3.1.1 Incompressible Flow

Assuming an incompressible flow ($\rho = constant$) and no external forces the mass and momentum equations in tensor notation become:

$$\frac{\partial U_i}{\partial x_i} = 0 \tag{3.6}$$

$$\rho\Big(\frac{\partial U_i}{\partial t} + U_j\frac{\partial U_i}{\partial x_j}\Big) = -\frac{\partial p}{\partial x_i} + \mu\Big(\frac{\partial U_i}{\partial x_j \partial x_j}\Big) \tag{3.7}$$

3.1.2 Euler Equations

The Euler Equations are a simplification of Navier-Stokes equation that consider the fluid as inviscid. This can be done setting $\mu = 0$ and so the Reynolds number $Re = \frac{\rho U L}{\mu} \to \infty$. In this way the following system for an incompressible flow is obtained:

$$\frac{\partial U_i}{\partial x_i} = 0 \tag{3.8}$$

$$\rho\Big(\frac{\partial U_i}{\partial t} + U_j\frac{\partial U_i}{\partial x_j}\Big) = -\frac{\partial p}{\partial x_i} \tag{3.9}$$

In a 2-dimensional coordinate system under steady conditions we get:

$$\frac{\partial u}{\partial x} + \frac{\partial v}{\partial y} = 0 \tag{3.10}$$

$$\rho\left(u\frac{\partial u}{\partial x} + v\frac{\partial u}{\partial y}\right) = -\frac{\partial p}{\partial x} \tag{3.11}$$

$$\rho\left(u\frac{\partial v}{\partial x} + v\frac{\partial v}{\partial y}\right) = -\frac{\partial p}{\partial y} \tag{3.12}$$

Since these equations describe an inviscid flow, the solution deviates from the true values in the area close to the wall. In addition, the Euler equations observe the wall boundary condition ($v_w = 0$) but no the no-slip condition ($u_w \neq 0$), so it is necessary to consider viscosity in the area near the wall to correctly describe the flow.

3.2 Boundary layer

The theory of boundary layer was invented and described by Ludwig Prandtl (1904) to take care of the velocity transition from the finite value near the wall to zero value at the wall. In this region the effects of viscosity are considered in order to satisfy the no-slip condition. This theory is applied to turbulent flows at high Reynolds number in order to simplify the treatment of the flows.
It divides the flow into two regions: an inviscid outer flow, which is the bulk of the flow region where effects of viscosity are neglected, and a thin boundary layer at the wall.

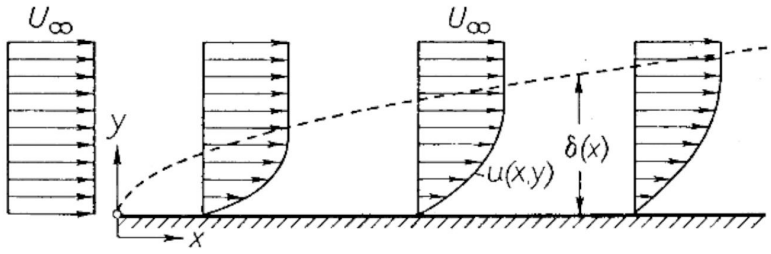

Figure 3.1: *Schematic representation of velocity distribution on a flat plate [37]*

In *Figure 3.1* a schematic representation of the velocity close to the wall is given. Velocity in the boundary layer is lower than the free stream velocity U_∞. Moreover it can be noted that the thickness δ of the boundary layer increases with the distance x from the leading edge of the plate. Since the concept of boundary-layer thickness is artificially introduced and often used, it is defined as the point where the velocity reach the 99% of the free stream value. For laminar boundary-layer the thickness can be calculated with the equivalence of viscous forces and inertial forces, obtaining:

$$\delta_{99}(x) = 5\sqrt{\frac{\nu x}{U_\infty}} \tag{3.13}$$

where ν is the kinematic viscosity.
In reality the boundary layer on a plate can become turbulent after a certain distance x_{crit} from the leading edge. This point can be calculated with the relation:

$$Re_{crit} = \left(\frac{U\, x_{crit}}{\nu}\right) \tag{3.14}$$

The critical Reynolds number is strongly dependent on how free from perturbation the outer flow is. A common value is $Re_{crit} = 5 \cdot 10^5$, if the flow is strongly perturbated $Re_{crit} = 3 \cdot 10^5$ is used, while for smooth flows $Re_{crit} = 3 \cdot 10^6$. Even though transition

from laminar to turbulent flow takes place in a region of finite lenght, transition point is used for simplicity. This transition becomes evident because of the increase of the boundary-layer thickness and the wall shear stress.

3.3 Turbulence

Turbulence is a flow condition in which velocity and pressure change chaotically in space and time while an average flow is maintained. It is three dimensional, unsteady complex process and consists of many scales. Turbulence occurs when viscous forces become less significant compared to inertial ones. Onset of turbulence can be predicted by the Reynolds number: high values, usually over 4000, are typical of turbulent flows. Eddies, vortices, and a reduction in drag are characteristics of turbulence due to the dominance of inertial forces.
In principle, the Navier-Stokes equations describe both laminar and turbulent flows without the need for additional information. However, turbulent flows at realistic Reynolds numbers span a large range of turbulent length and time scales and so they are treated using statistical models on the fluctuating turbulent component of the flow variables.

Chapter 4

Methodology

The aim of this chapter is to describe the model used for the present analysis, specify the methods and justify design choices.

4.1 Model geometry

The idealized geometry of the upper respiratory tract has been designed using the commercial software Rhinoceros version 7 (Robert McNeel and Associates, Seattle, WA, USA), starting from the one proposed by Huang & Zhang (2011) [21].
The model present an upper oral tract arc shaped, followed by the restricted zone of the larynx and a straight tube for the trachea. The bronchial bifurcations are designed to be asymmetrical, with three lobes on the right side and two on the left. For sake of simplicity, "out-of-plane" bifurcations are not considered. In the *Figure 4.1* the model for the healthy airways is shown from a frontal point of view with all the measures listed. The stenotic and stented airways are modeled starting from this geometry, modifying the trachea, the carina and a part of the left and right first bronchial tubes.
Five designs of stenotic trachea are made (*Figure 4.2*): three with a symmetrical reduction of the 20%, 30% and 50% respectively of the trachea diameter in the middle section, one with an asymmetrical but still circular 50% stenosis and the last one with an asymmetrical elliptical stenosis.
As regard the airways with prosthetic device it has been chosen to investigate both the case with Dumon tracheal stent and Y carinal stent. The simulations were carried out with devices of 1mm and 1.5mm of thickness. In the *Table 4.1* are listed the measures of the used devices. For sake of simplicity the *Figure 4.3* shows just the devices with thickness of 1.5mm since the difference with the airway wall is more evident.

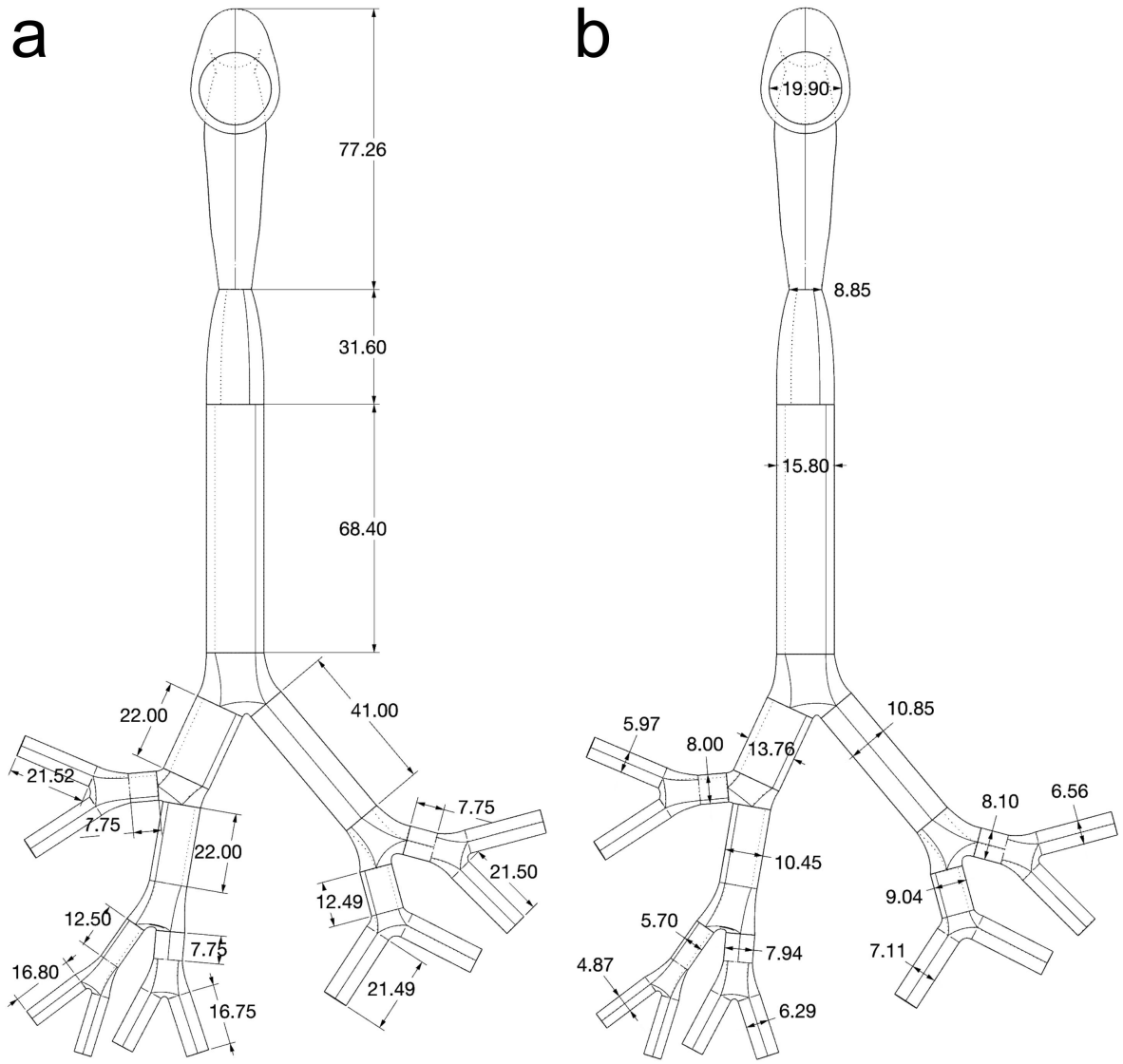

Figure 4.1: *Frontal view of the healthy airways model: (a) measures of the length of the vessels tube, (b) diameters of the tubes*

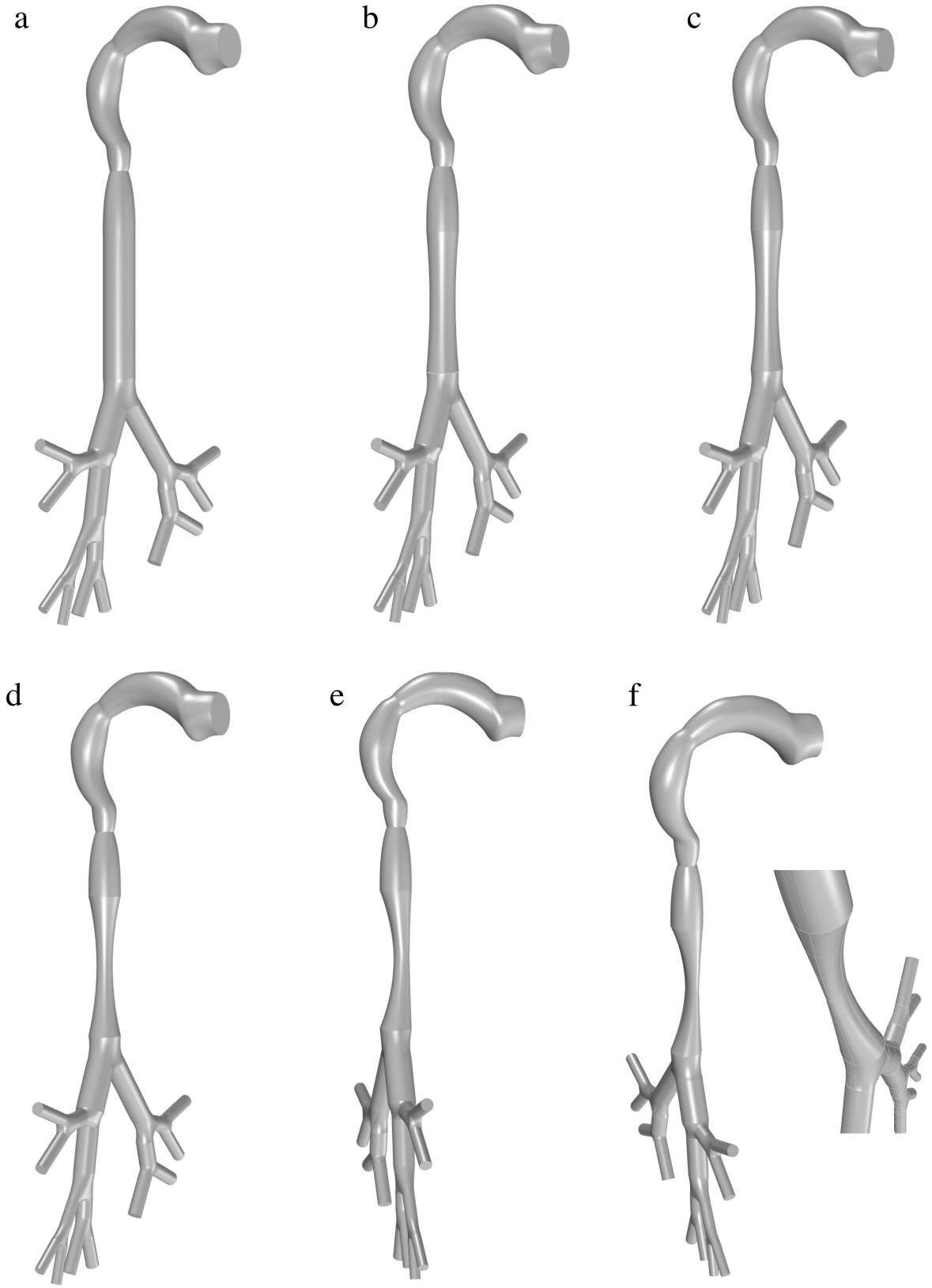

Figure 4.2: *(a) healthy airways model; symmetrical stenotic airways model with (b) 20% reduction, (c) 30% reduction, (d) 50% reduction in diameter; (e) asymmetrical circular stenosis; (f) asymmetrical elliptical stenosis with detail*

	Thickness [mm]	Length [mm]
Dumon stent	1	40
	1.5	40
Y stent	1	40/15/15
	1.5	40/15/15

Table 4.1: *Main dimensions of the considered prosthetic devices (the three dimensions given for the Y stent refers to the length of the three segments of the device)*

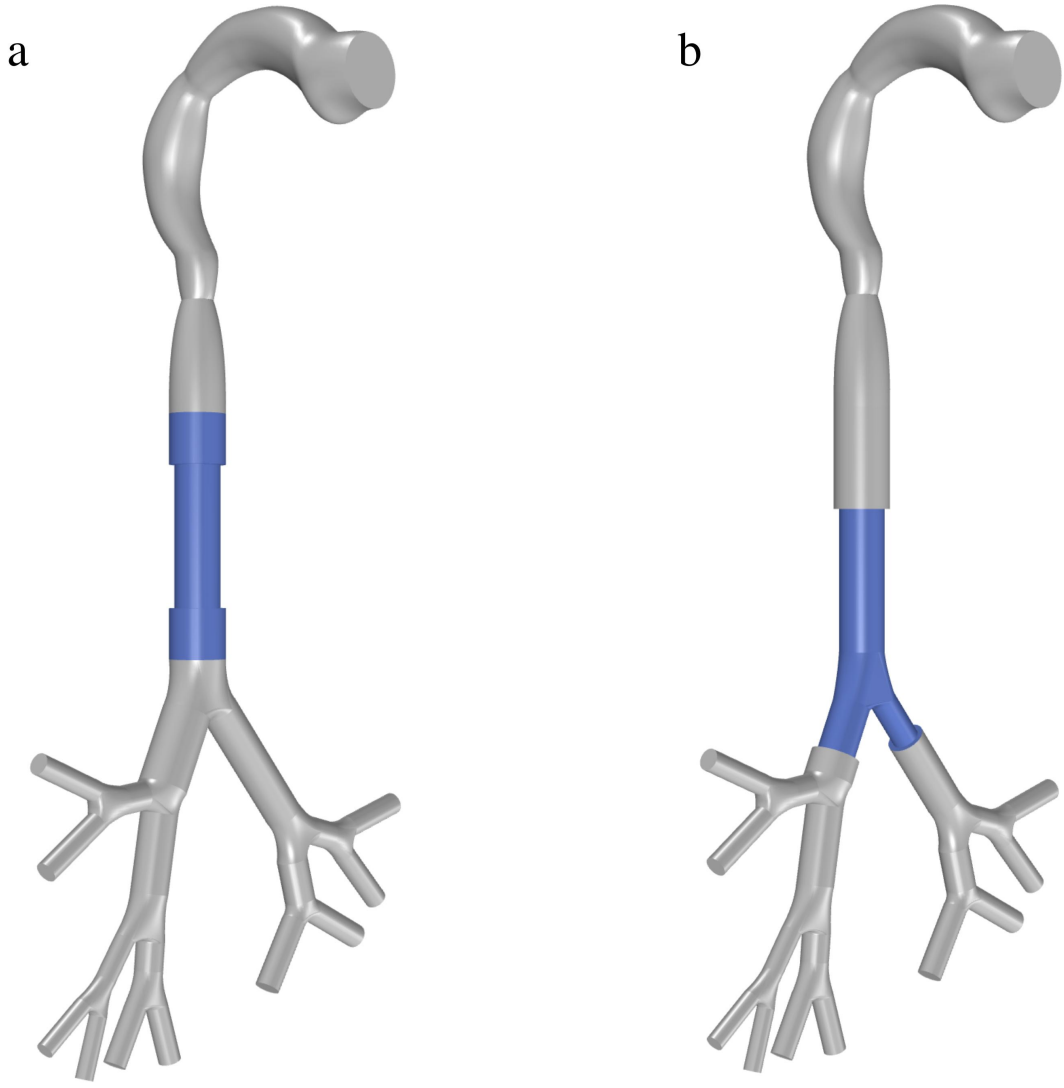

Figure 4.3: *Stented airways: (a) Dumon stent and (b) Y stent are represented in blue*

4.2 Discretization

The meshing process has been done with the software Ansys ICEM CFD 2020 R2 (ANSYS Inc., Canonsburg, Pennsylvania).
Through the Octree method an unstructured tetrahedral mesh is obtained. This algorithm uses a top-down approach, ensuring good refinement where it is necessary, and maintains larger elements in the central part to allow faster computation. In this case it has been chosen to keep the maximum element size at 1mm and a refinement down to 0.5mm on curve surfaces.
Moreover it has been decided to use a prism discretization in the near-wall region to simplify the convergence of calculation in the boundary layer. This prism section consists of five layers for a total height of 0.5mm.
Last step was extruding the inlet surface for 20mm to create the "mouth tract" that allows the flux to enter the oral tract with a uniform distribution of particles and velocity and ensures the convergence of the simulation.
The grids obtained in this way have 1 million nodes and 3 millions elements, which have been proven to give good results with respect to overall computational time [20].

Table 4.2: *Mesh characteristics for the different models*

Model	Nodes	Elements
Healthy	1068507	3010977
Dumon stent 1mm	1057892	2970508
Dumon stent 1.5mm	1052832	2952285
Y stent 1mm	1045877	2930852
Y stent 1.5mm	1032402	2884240
Stenosis 20%	1048156	2938677
Stenosis 30%	1039713	2904556
Stenosis 50%	1019211	2832349
Asymmetric circular stenosis	1021218	2840447
Asymmetric elliptical stenosis	1023078	2845254

4.3 Governing equations

4.3.1 Transport equations

To account for turbulence, the Reynold Averaged Navier-Stokes (RANS) equations are modeled employing the eddy viscosity and eddy diffusivity hypothesis. The first states that Reynold stresses can be related to the mean velocity gradient and eddy viscosity (ν_t), the second assumes that the Reynold fluxes of a scalar are linearly related to the

mean scalar gradient through the eddy diffusivity $\Gamma_t = \frac{\nu_t}{Pr_t}$, where Pr_t is the turbulent Prandtl number. Hence for viscous, isothermal and incompressible flow the continuity and momentum equations become:

$$\nabla \cdot \mathbf{u} = 0 \tag{4.1}$$

$$\frac{\partial \mathbf{u}}{\partial t} + \nabla \cdot (\mathbf{u} \otimes \mathbf{u}) = -\frac{1}{\rho}\nabla p' + \nabla \cdot (\nu_{eff} \left(\nabla \mathbf{u} + (\nabla \mathbf{u})^T\right)) \tag{4.2}$$

where $\mathbf{u}$ is the average fluid velocity vector, ρ is the fluid density, p' is the modified pressure (which is assumed equal to pressure in the default solver of Ansys-CFX), ν_{eff} is the effective kinematic viscosity and it is defined as the sum of fluid kinematic viscosity $\nu = \frac{\mu}{\rho}$ and turbulence kinematic viscosity $\nu_t = \frac{k}{\omega}$; k and ω are the turbulence kinetic energy and turbulent frequency respectively. To calculate them the k-ω-based Shear Stress Transport model of turbulence has been adopted. It uses a blending function based on flow variables and distance from the nearest surface. A detailed description of the SST model is given in the Appendix B.

4.3.2 Particle transport

The particle tracking is performed in a Lagrangian reference since micro-particles are considered as dilute monodisperse rigid sphere suspension with low volume fraction of particle phase.
The particle trajectories are calculated integrating the particle velocity over time. The velocity is given by the force balance:

$$\sum F = m_p \frac{d\mathbf{u}_p}{dt} \tag{4.3}$$

where F is the force term and $\mathbf{u}_p$ the velocity of the particle.
Because of the assumptions made on the particles most of the force terms of the momentum equation (4.3) can be neglected, obtaining:

$$m_p \frac{d\mathbf{u}_p}{dt} = \frac{1}{8} d_p^2 \pi \rho C_D |\mathbf{u} - \mathbf{u}_p|(\mathbf{u} - \mathbf{u}_p) \tag{4.4}$$

where $\mathbf{u}$ and ρ are the fluid velocity and density respectively, and C_D is the drag coefficient calculated with Schiller-Neumann model:

$$C_D = max\Big(\frac{24}{Re_p}(1 + 0.15 Re_p^{0.687}), 0.44\Big) \tag{4.5}$$

where Re_p is the particle Reynolds number.

4.4 Simulations setup

All simulations have been carried out using Ansys CFX 2020 R2 (ANSYS Inc, Canonsburg, Pennsylvania), a well-known software for fluid dynamics computations, on an Intel Core i9 processor. For each simulations the computational time was about 30 minutes.

4.4.1 Fluid domain

The fluid domain under study consists of two materials: air and aerosol.
The first was assumed incompressible and Newtonian fluid with $\rho = 1,185 kg/m^3$ and $\mu = 1,831 \cdot 10^{-5} kg/(m \cdot s)$. Instead the aerosol ($\rho = 1000 kg/(m \cdot s)$) consist in fluid spherical particles, whose diameter varies between 1 and 15 μm depending on the simulation. Since particles are sufficiently small and diluted, one-way coupling has been selected. In this way the airflow field was evaluated first and then the particle trajectories were computed. The simulations are carried out in isothermal condition at a temperature of 25 °C .
Even if the flow is laminar at the inlet in most of our cases, turbulence may occur locally and rapidly rises in constriction zones (as at the larynx). As turbulence model the Shear Stress Transport has been chosen because it accounts for the transport of turbulent shear stress provoked by the particles and give very accurate predictions on the onset and the amount of flow separation under adverse pressure gradient. The SST model is based on the Wilcox $k - \omega$ model, well-known for having a more robust and accurate treatment of the near wall situation than the $k - \epsilon$ model.

4.4.2 Boundary conditions

Boundary conditions are crucial for the outcome of the simulations.
The airways walls were assumed to be smooth and rigid with a non-slip condition. Smoothness of the walls allows to simulate the direct deposition of particles (when the distance of the particle center from the wall is less than the radius of the sphere), as it happens in the real airways because of the presence of mucus.
At the outlets the relative Average Static Pressure on Whole Outlet was imposed ad 0 Pa.
At the inlet steady constant flow rates were imposed: 15 L/min, 30 L/min, 45 L/min and 60 L/min for the healthy model in order to compare the results with the literature and validate the model; 6 L/min, 9 L/min and 90 L/min for the stenotic models and 12 L/min, 18 L/min and 180 L/min for the stented models. 90 L/min and 180 L/min represent the maximum flow rate during spirometry test of stenotic and post-operatory patients respectively (Malvè *et al.*, 2013) [26]. Comparing these flow rates with the healthy one

(8 L/s), it has been decided to investigate smaller flow rates to simulate light and normal breathing conditions.
2000 particles were injected uniformly at the inlet for each simulation.

Table 4.3: *Inlet velocity values for the different flow rates*

	Flow rate [L/min]	Inlet velocity [m/s]
healthy flow rates	15	0.8044
	30	1.6088
	45	2.4132
	60	3.2176
	480	25.7408
stenotic flow rates	6	0.3218
	9	0.4827
	90	4.8270
stented flow rates	12	0.6436
	18	0.9654
	180	9.6540

4.4.3 Convergence criteria

In engineering field, where most of the problems are solved in a numerical iterative way, the choice of the right *convergence criteria* is fundamental. It is usually a compromise between computational time and results accuracy, which depends on the purpose of the analysis.
One of the most used criteria, and the one chosen for this analysis, is the evaluation of *root mean squared* (RMS) residuals. Since Ansys CFX uses an iterative method to solve the simulation, at each step the RMS residuals directly quantify the error in the solutions of the system equation. This value can never be exactly zero, but can fall below a threshold set by the user.
In this study the solution of the flow field was considered converged when the RMS residuals are less than 10^{-6}. This value is largely used in the literature of particle deposition and airways flow study ([16]).

Chapter 5

Discussion of results

The aim of this chapter is to present and discuss the results obtained with the support of images and graphs.

5.1 Model validation

Before analysing the stenotic and stented model outcomes it is necessary to evaluate if the model built can describe correctly the airflow and particle transport in the upper airways. In order to validate the model some simulations are carried out through the healthy model and the results are compared to the ones published in literature.
As already stated, the used fluxes are 15, 30, 45 and 60 L/min. In *Figure 5.1* the velocity profiles are shown at mid cross-section of the oral tract and the tracheobronchial tree. Velocity contours and magnitude are in good agreement with the results of Rahimi-Gorji *et al.* [34] for a healthy model obtained from a CT scan. At all flow rates the airflow is skewed in the posterior wall of the oral tract due to centrifugal force and this leaves space to a recirculating zone where secondary flows arise. The main difference with the CT-based model used by the authors is the direction of the laryngeal jet: while in their work it is deflected towards the frontal part of the trachea, in the present case the airflow is bounced to the back wall. The same difference can be found also with the velocity profiles obtained by Huang *et al.* [20]. An explanation to this phenomenon may be different geometrical angles between the curve section of the oral tract and the larynx part. Anyway, from the frontal point of view, the flow bounces from the right wall to the left as predicted by Zhang *et al.* [47].

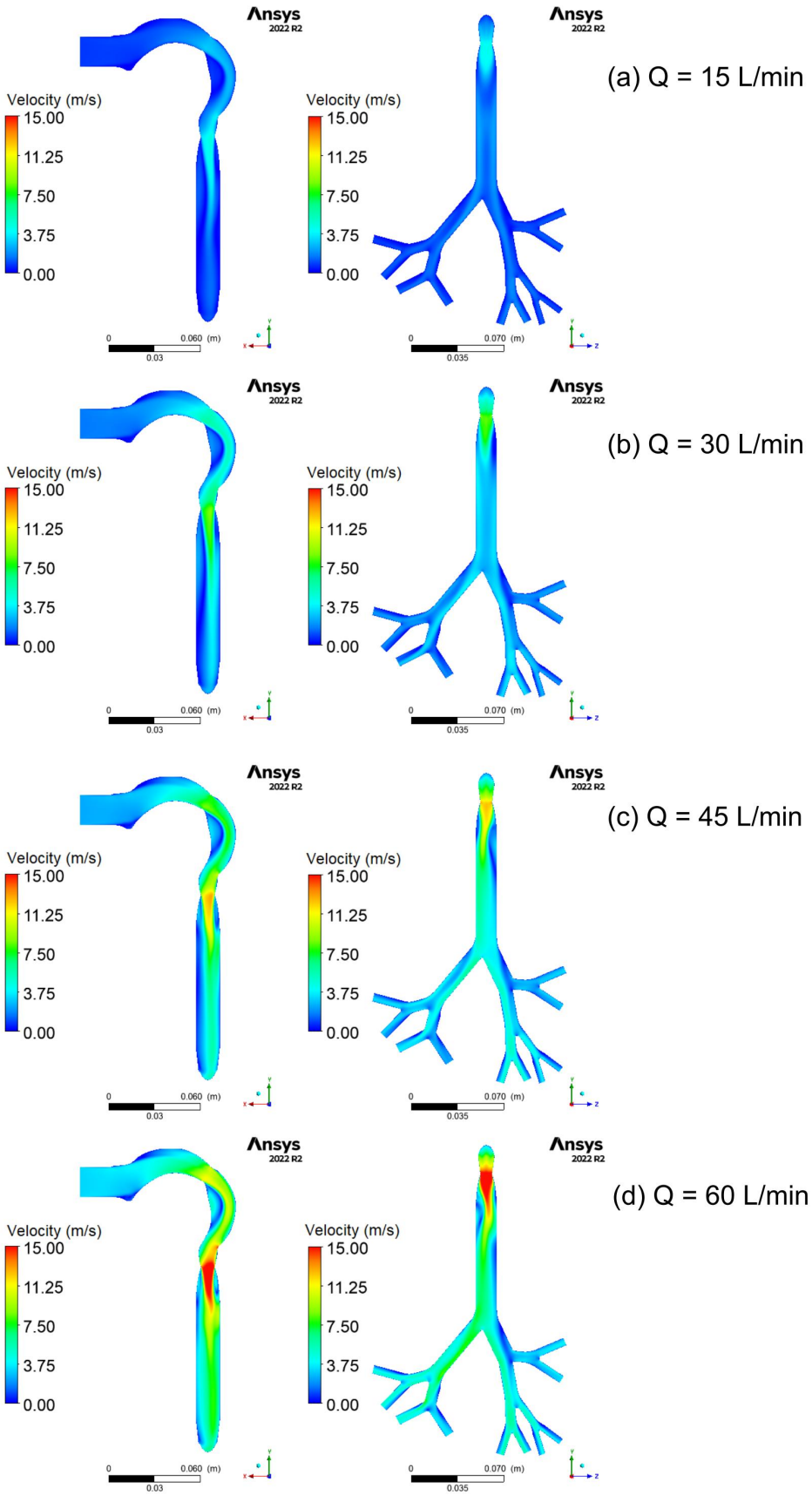

Figure 5.1: *Velocity magnitude contour at mid cross-section in the healthy model for different flow rates*

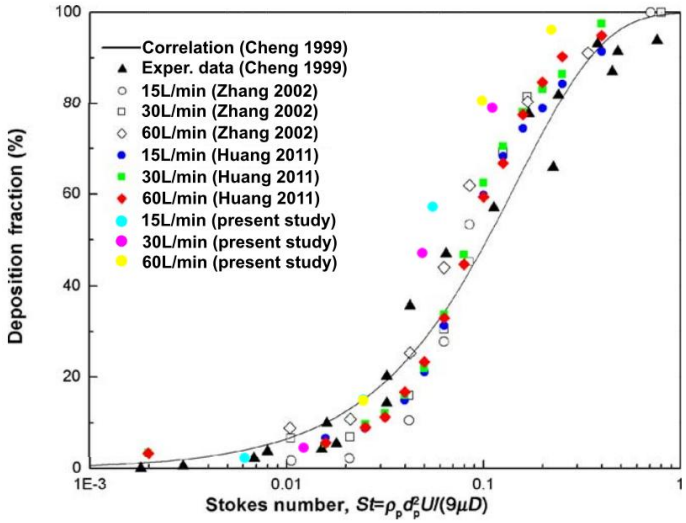

Figure 5.2: *Deposition fraction in the oral airways as a function of the Stokes number.*

Particle transport and deposition is evaluated through the value of the deposition factor, defined as the ratio of particles deposited on a specific surface to the total particle number entering the mouth inlet:

$$DF = \frac{particle\ number\ deposited\ on\ the\ surface}{total\ particle\ number\ entering\ the\ mouth\ inlet} \tag{5.1}$$

Considering the deposition fractions in the upper oral tract a correspondence with previous works [8, 47] can be found in the relation between DF and Stokes number, calculated as $St = \frac{\rho_p d_p^2 \bar{U}}{9\mu D}$, where $\bar{U}$ and D are the velocity of the flow at the inlet and the inlet diameter respectively (*Figure 5.2*). Moreover the trend of the correlation between DF and the Impaction Parameter ($IP = d_p^2 Q$ expressed in μm and L/min respectively) has been evaluated and compared with literature data in *Figure 5.3*.

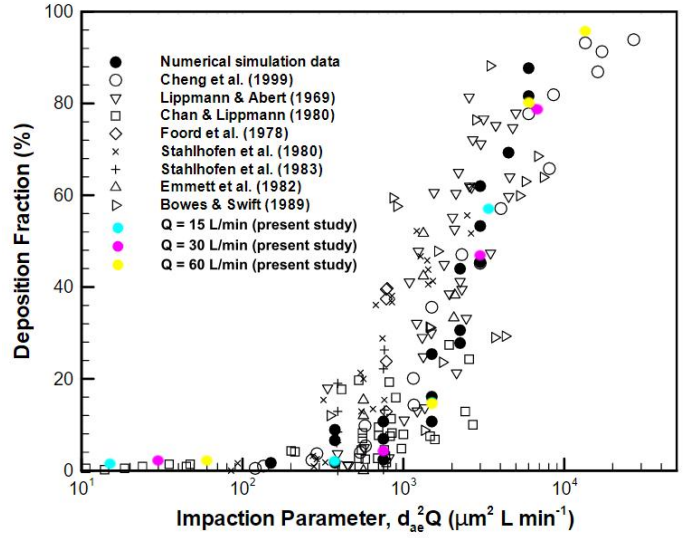

Figure 5.3: *Comparison of simulated deposition particles with in vivo and in vitro experimental results.*

As regard the tracheobronchial section, a comparison of the results can be done with the works of Schlesinger *et al.* [36], Rahimi-Gorji *et al.* [35, 34], Chen *et al.* [5], Huang *et al.* [20], Kleinstreuer *et al.* [22], Malvè *et al.* [27] and much more authors. While the velocity magnitude comparison was both qualitative and quantitative, in this case the percentages of deposited particles are not corresponding because of the presence of an oral tract and little geometrical differences in the model. It has been proven by Zhang *et al.* [48] that a big percentage of large micro-particles tends to deposit in the pharynx as an effect of soft palate and bending of the airways, and so deposition data for tracheobronchial airways are accurate only when this upper part is considered. This explains why in *Figure 5.6* the DF of bigger particles are significantly lower in the case of a flow rate of 60 L/min with respect to 30 L/min.

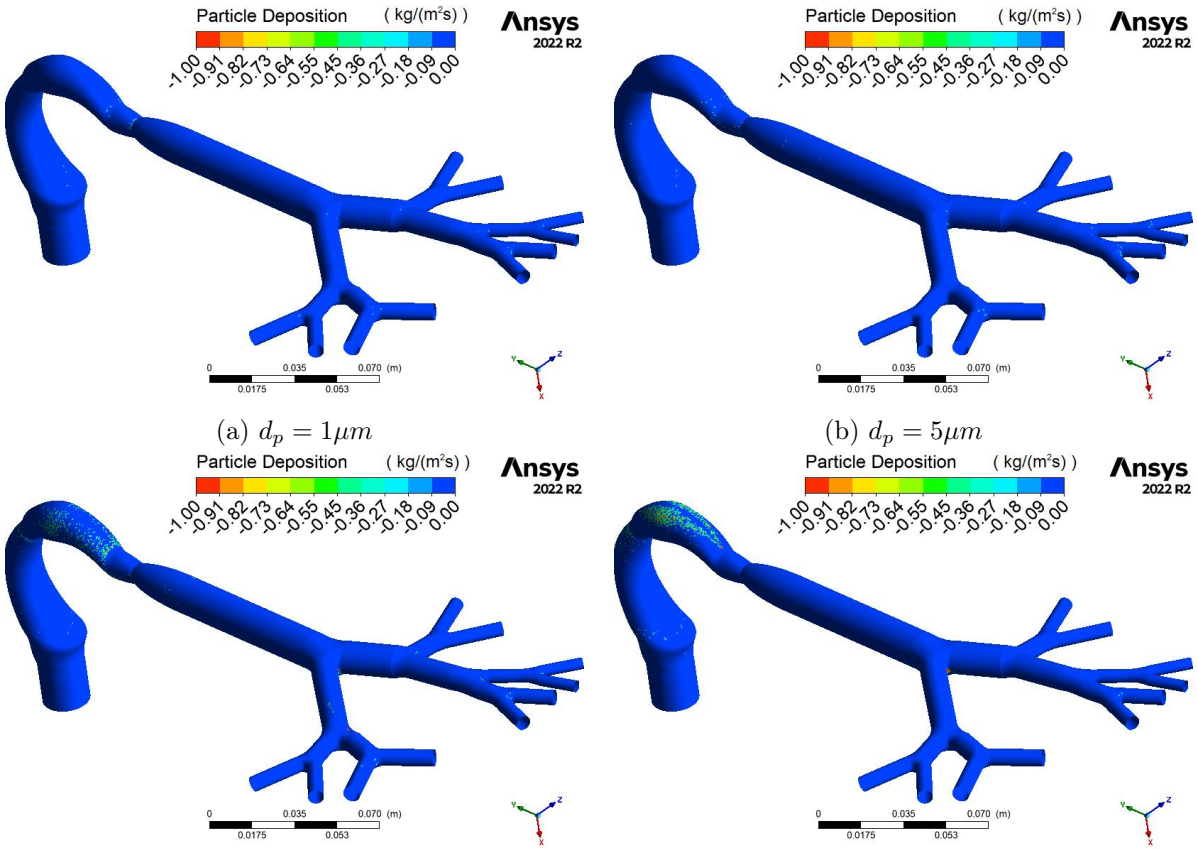

(a) $d_p = 1\mu m$ (b) $d_p = 5\mu m$

(c) $d_p = 10\mu m$ (d) $d_p = 15\mu m$

Figure 5.4: *Particle deposition in the healthy model at flow rate Q = 30 L/min and different particle diameters*

A graphical representation of particle deposition is given in *Figure 5.4* for breathing flow rate of 30 L/min. Enhanced deposition at bifurcation with respect to straight tubes can be noticed, as well as the high deposition of big particles in the pharyngeal region. The

null deposition zone in the midst of accumulated deposition in oral tract is the effect of the uvula on velocity. In fact, from the velocity contour, a lower-speed zone can be detected at the posterior wall of the oral tract. For particles of 1 and 5μm diameter, deposition is more scattered, indicating an higher effect of turbulence on small particles. It is also important to notice that deposition tends to occur mainly at the carinal ridge due to inertial impaction mechanism, confirming the presence of "hot spots" stated by Schlesinger [36] ad Zhang [48].
For low flow rates deposition is almost null for small particle while bigger ones tend to deposit in the oral tract. Increasing the flow rate, a significant deposition on the left bronchus can be noticed: this happens because of the centrifugal force induced in the subsequent curvature of the left branch. This same result has been obtained by Rahimi-Gorji *et al.* [34] and confirmed by Cai *et al.* [4], who studied the effect of bifurcation angle on deposition.

In conclusion the overall deposition factors are similar to the ones found in literature.

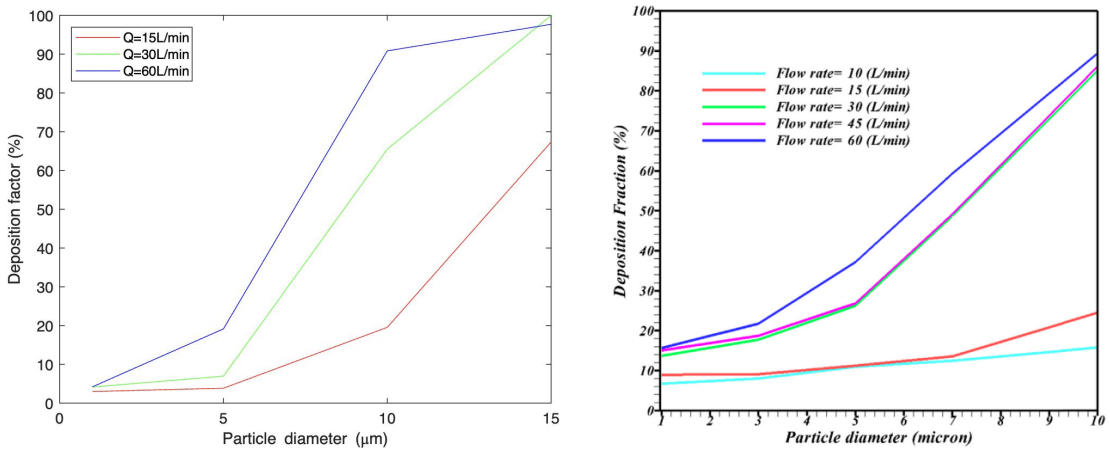

(a) *Present work* (b) *Rahimi-Gorji et al. (2016)*

Figure 5.5: *Overall deposition factor in the healthy airways for different particle diameters.*

Figure 5.6: *Deposition fraction in the healthy tracheobronchial tree*

Last step of the validation process has been the evaluation of the number of used particles on the deposition. From the histograms shown in *Figure 5.7* it can be stated that there is no influence of the number of particles on the DF of the model and so the number of 2000 particles has been chosen for computational reasons.

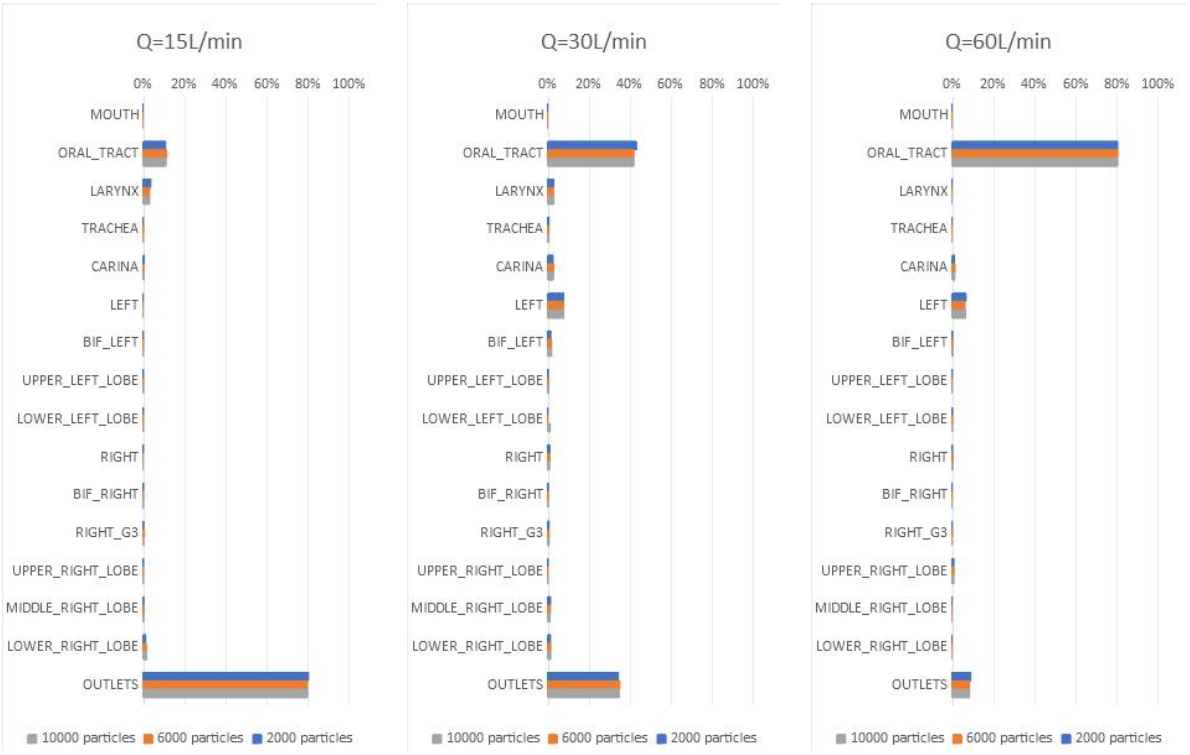

Figure 5.7: *Comparison between different number on injected particles on the deposition factors*

5.2 Stenotic airways

The increasing number of COPD affected patients encourages the researcher to focus their attention on the analysis of airflow and particle deposition in the human airways. Several works on obstructed airways have been published in the last years, such as the one of Yang *et al.* [44], Luo *et al.* [25], Brouns *et al.* [3], Chen *et al.* [6], Malvè *et al.* [26], Sul *et al.* [40], Farkhadnia *et al.* [16], Zhang *et al.* [45]. In most of these studies the Weibel model has been employed, considering the effect of an obstruction on symmetrical branching. Since the present work uses an asymmetrical model, still idealized but more realistic, it is to be hoped that the results could help improving the understanding of air and particle dynamics in diseased lungs in order to enhance drug aerosol therapies.

5.2.1 Different degrees of stenosis

Small particles (1-5 μm) deposition at low flow rates is almost null at every degree of stenosis and around 95% of them reach deeper lung regions. The small amount of deposited particles is usually on the oral tract or at the carinal ridge. Moreover 1 μm particles can reach lower bronchial regions also in the case of forced rapid ispiration as in the case of spirometry test. On the other hand, larger particles (10-15 μm) deposit mainly at the pharynx level for high flow rates.

In the present study 9 L/min has been considered as a normal breathing flow rate for patients with stenotic trachea. In fact patients with tracheal stenosis show breathing impairment and, as a consequence, a significantly inferior value of flow rate needs to be used with respect to the healthy one. It has also been investigated the airflow and particle transport for flow rate of 6 L/min but the outcome is not really significant for low degrees of stenosis since it is not realistic that a patient with a slightly stenotic trachea has that breathing impairment. From the velocity profiles of *Figure 5.8* it is evident that in the case of more obstructed trachea, the flow is faster and tends to enter more the right bronchus because it is less deflected. Higher velocity and flow direction explain the higher deposition on the carina and in the right lobes.

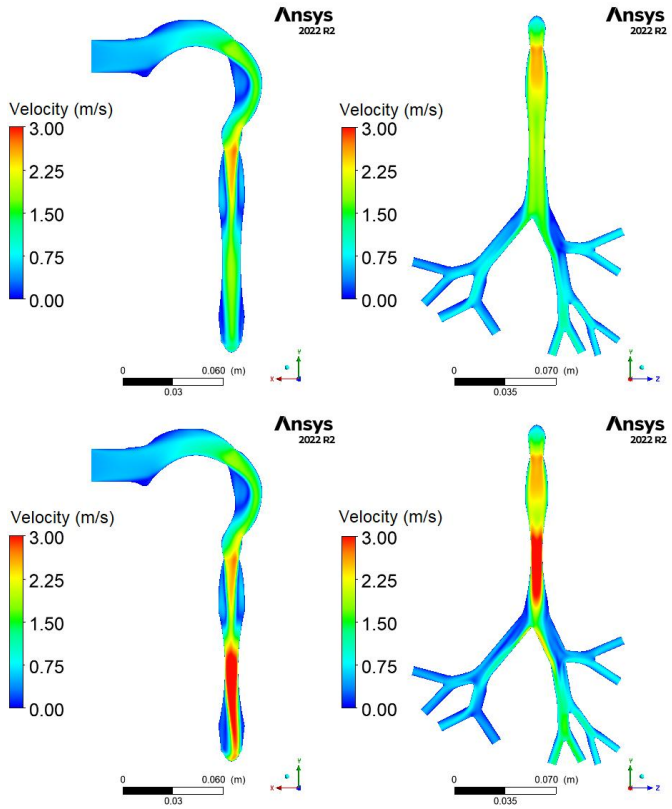

Figure 5.8: *Velocity contours for a flow rate of 9 L/min in the model with stenosis of 30% (upper panel) and 50% (lower panel).*

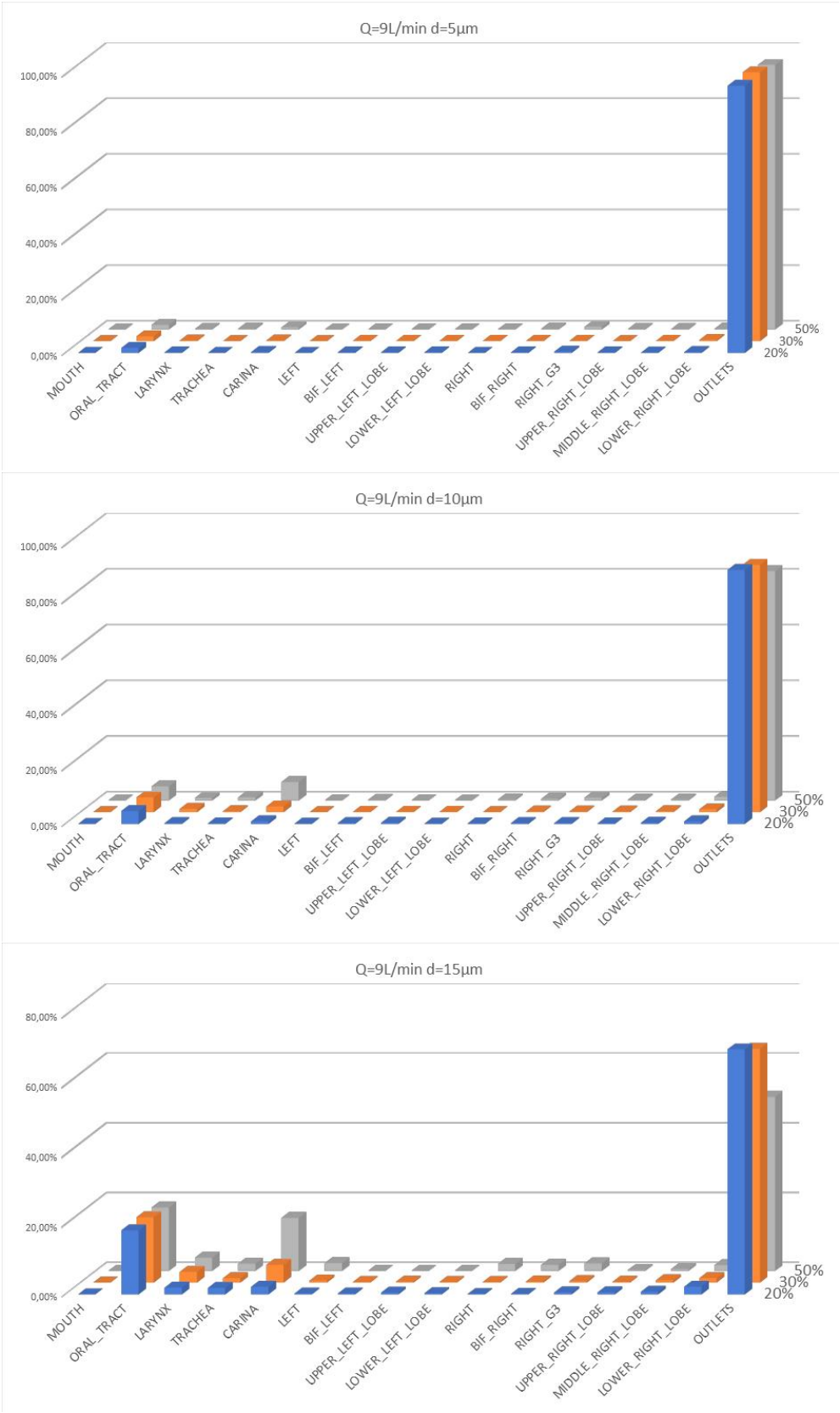

Figure 5.9: *Comparison of deposition fraction in the diseased airways at different degrees of stenosis for flow rate of 9 L/min and particle sizes of 5, 10 and 15 µm*

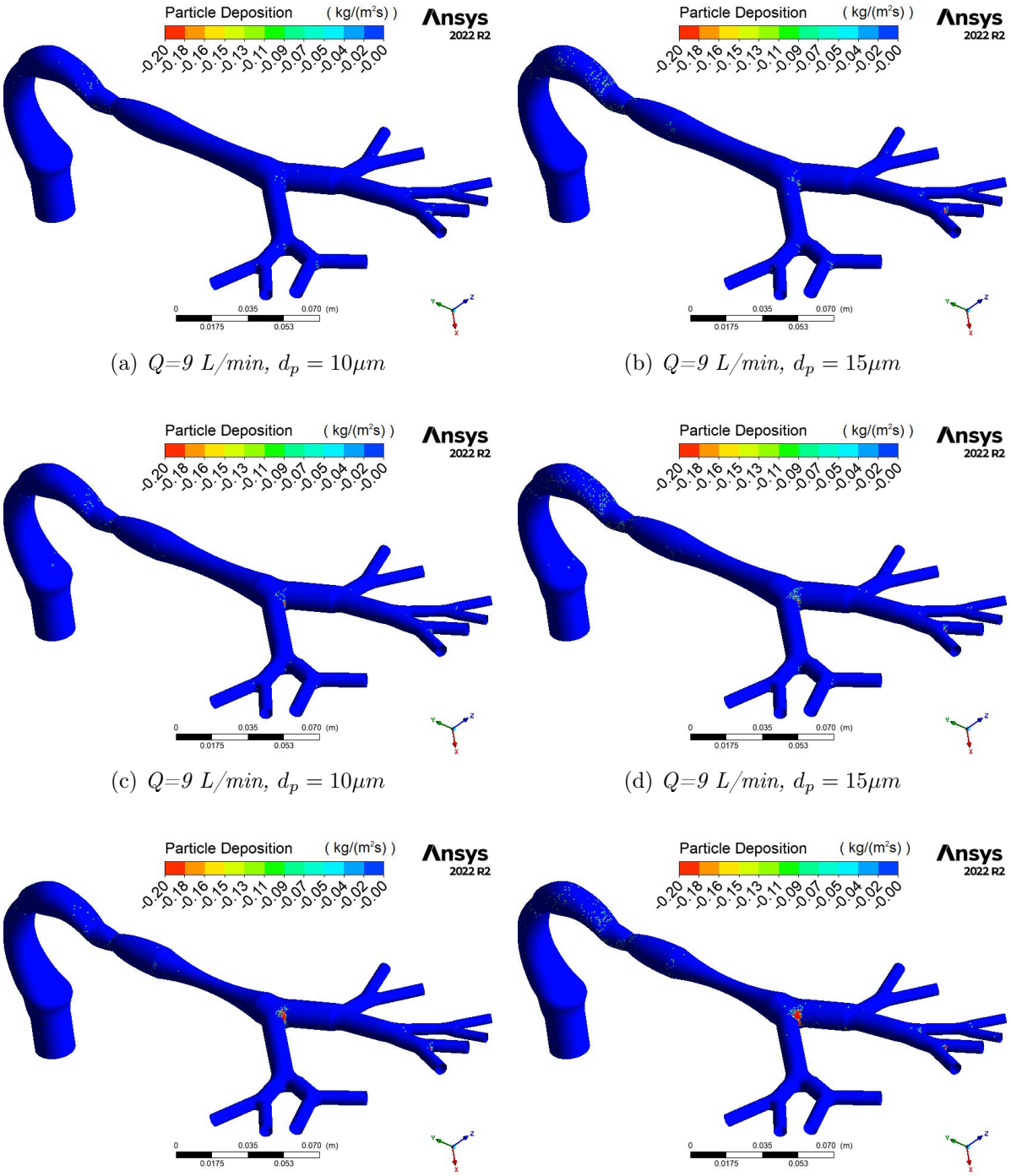

(a) Q=9 L/min, $d_p = 10\mu m$

(b) Q=9 L/min, $d_p = 15\mu m$

(c) Q=9 L/min, $d_p = 10\mu m$

(d) Q=9 L/min, $d_p = 15\mu m$

(e) Q=9 L/min, $d_p = 10\mu m$

(f) Q=9 L/min, $d_p = 15\mu m$

Figure 5.10: *Particle deposition in the obstructed model with a degree of 20% (first row), 30% (second row) and 50% (third row) of stenosis in the trachea at the flow rate of 9 L/min.*

In *Figure 5.9* and *Figure 5.10* a comparison of deposition fractions is shown both in a quantitative and qualitative way. Deposition on the oral tract increase with particle size and it is not affected by the degree of stenosis, while deposition of particles in the larynx, trachea and the carinal ridge is intensified for bigger particles.

Graphical representation of deposition in *Figure 5.10* confirms increased deposition on the bifurcation after the obstruction with respect to the healthy as in the study of Chen *et al.* [6]. Moreover deposition on the surface of the obstructed trachea is quite relevant for bigger particles and usually happens in the surface before the constriction because of the recirculation generated by the shrinking of the flow in the narrow trachea.
Graphs in *Figure 5.11, 5.12* show clearly DF increasing with the degree of stenosis. The low value for tracheal DF of $5\mu m$ particles in case of spirometry for the model with a 30% stenosis is due to the fact that DF is high for the larynx region (2.45%) with respect to the data for other models, and depend on the empirical segmentation of the airways.

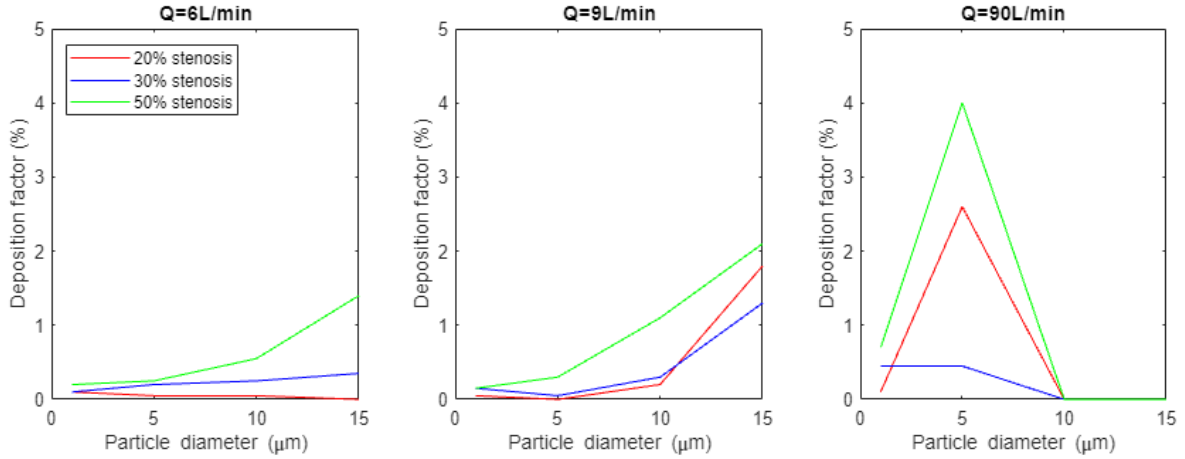

Figure 5.11: *Comparison of deposition fraction in the trachea at different degrees of stenosis for different flow rates.*

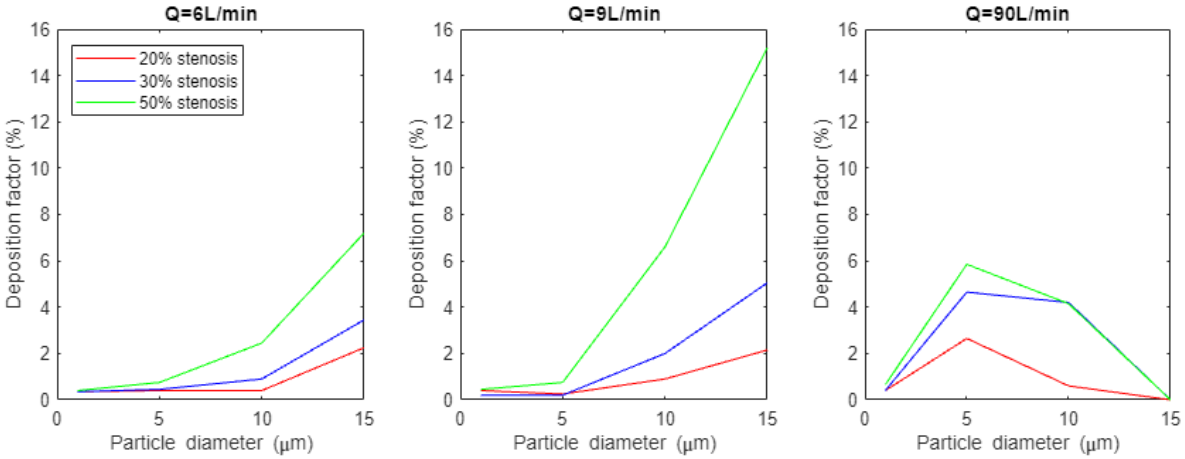

Figure 5.12: *Comparison of deposition fraction in the carina at different degrees of stenosis for different flow rates.*

Understanding particle transport and deposition is crucial to improve drug aerosol therapies. In this perspective, it is useful to investigate deposition at high flow rate representing forced inspiration. From spirometry test [26], 1.5 L/s is the maximum inspiration rate for a stenotic patient. Under this breathing conditions, for all degrees of stenosis, $1\mu m$ particles tend to reach deeper lung regions and bigger particles in this analysis deposit on the pharynx.

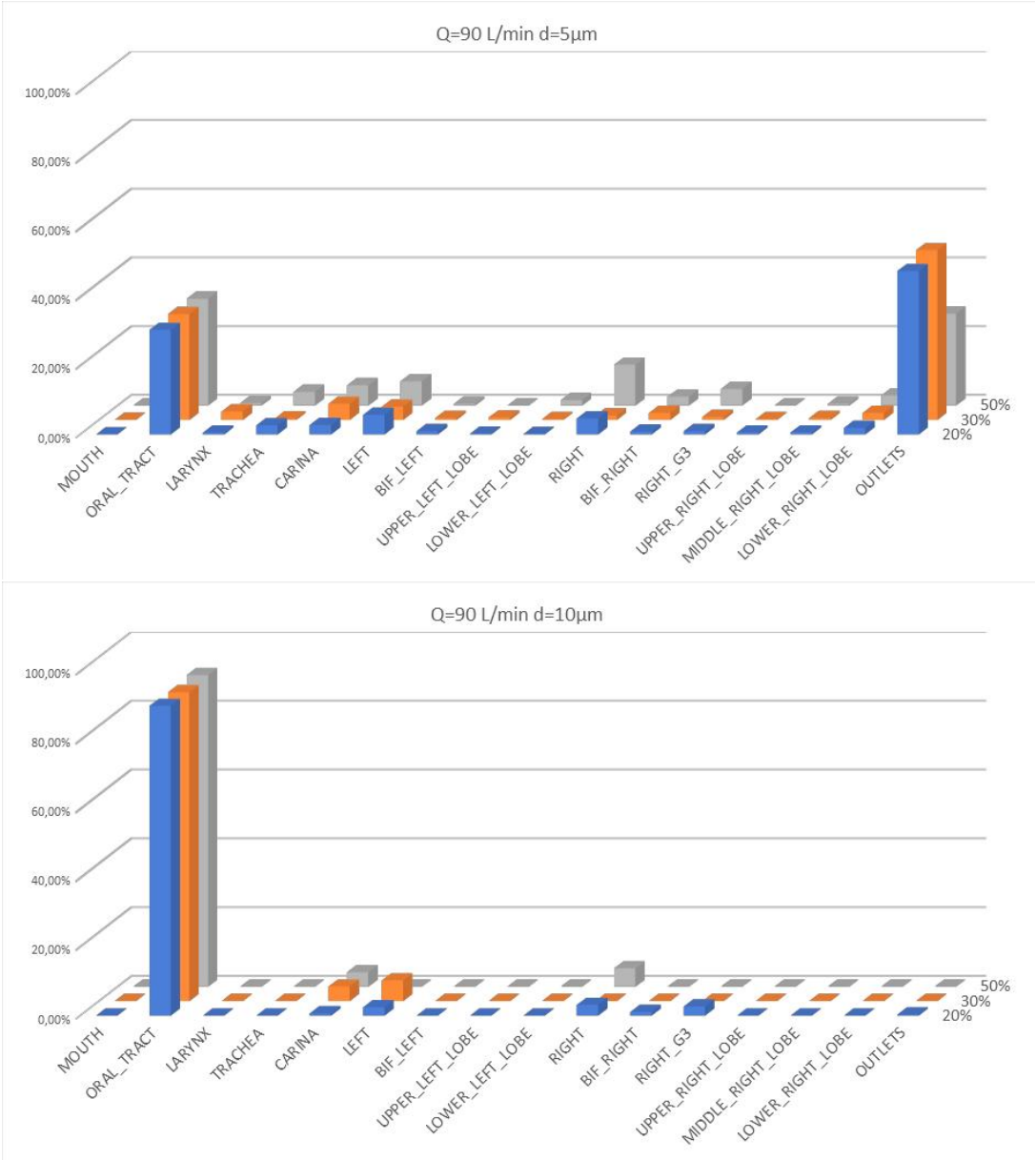

Figure 5.13: *Comparison of deposition fraction in the airways model at different degrees of stenosis for flow rate of 90 L/min and particle sizes of 5 and 10 µm*

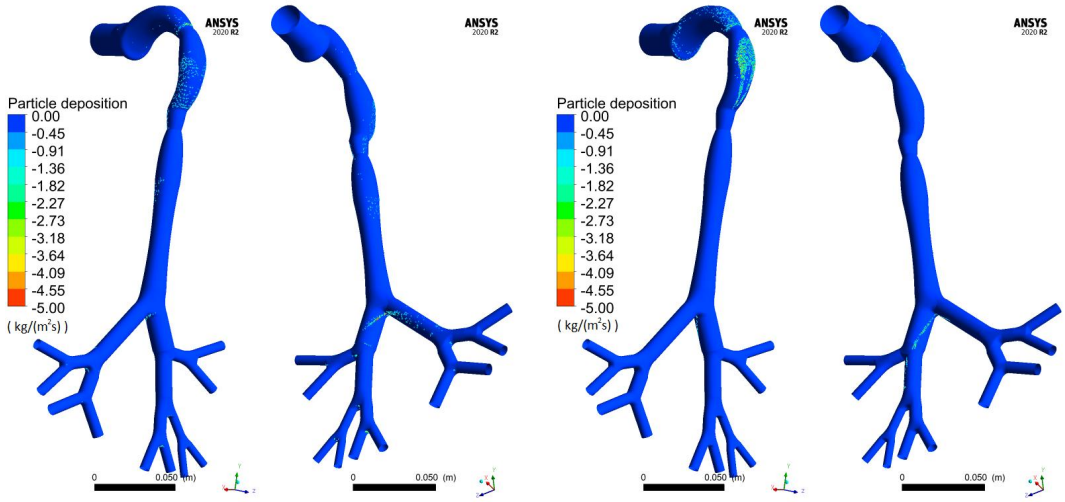

(a) Q=90 L/min, $d_p = 5\mu m$ (b) Q=90 L/min, $d_p = 10\mu m$

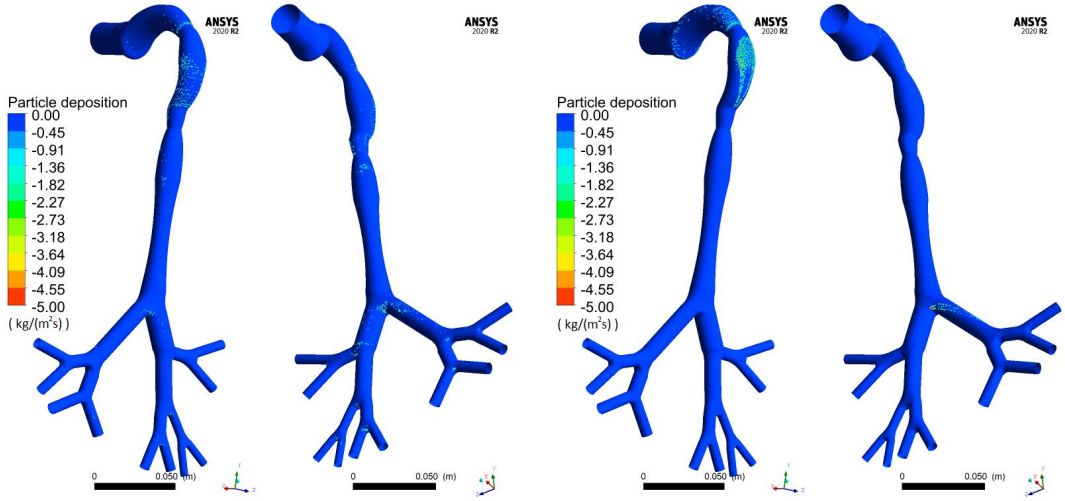

(c) Q=90 L/min, $d_p = 5\mu m$ (d) Q=90 L/min, $d_p = 10\mu m$

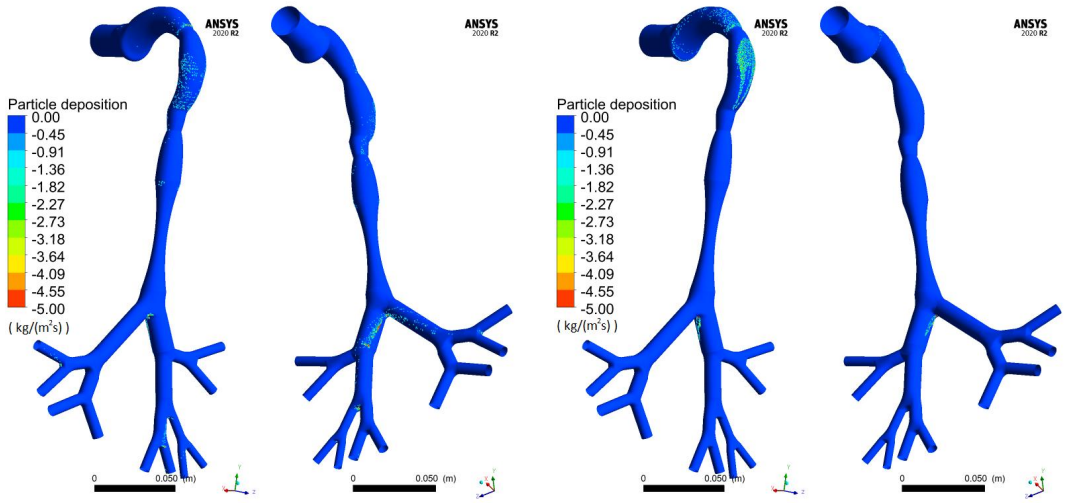

(e) Q=90 L/min, $d_p = 5\mu m$ (f) Q=90 L/min, $d_p = 10\mu m$

Figure 5.14: *Particle deposition in the obstructed model with a degree of 20% (first row), 30% (second row) and 50% (third row) of stenosis in the trachea at the flow rate of 90 L/min.*

It can be noted from both histograms (*Figure 5.13*) and graphical representation (*Figure 5.14*) that $10\mu m$ particles deposit also on the carinal ridge but still do not reach the outlets. Deposition of $5\mu m$ particles is more dispersed across the whole airway: a significant percentage of particle deposit in the oral tract and less than half of the particle entering the inlet can reach outlet. Deposition of particles in trachea, carinal ridge and right lobe are remarkable, especially for a high degree of stenosis but still significant also at lower levels. In healthy lungs deposition tend to be higher in the left lobe because of the higher bifurcating angle in that branch; on the contrary the stenosis tend to re-adjust the flow to the center line and so it flows in the tube with less deflection.

5.2.2 Symmetrical and asymmetrical stenosis

So far, all obstructions have been modeled as a circular symmetrical narrowing of the tube. In the present work a comparison between this idealized stenosis and two asymmetrical ones with the same area has been carried on. Results for particles with diameter of 10 and 15 μm are showed in *Figure 5.16* for normal inhalation rate and *Figure 5.17* shows the DF of 5 and $10\mu m$ particles for forced inspiration.

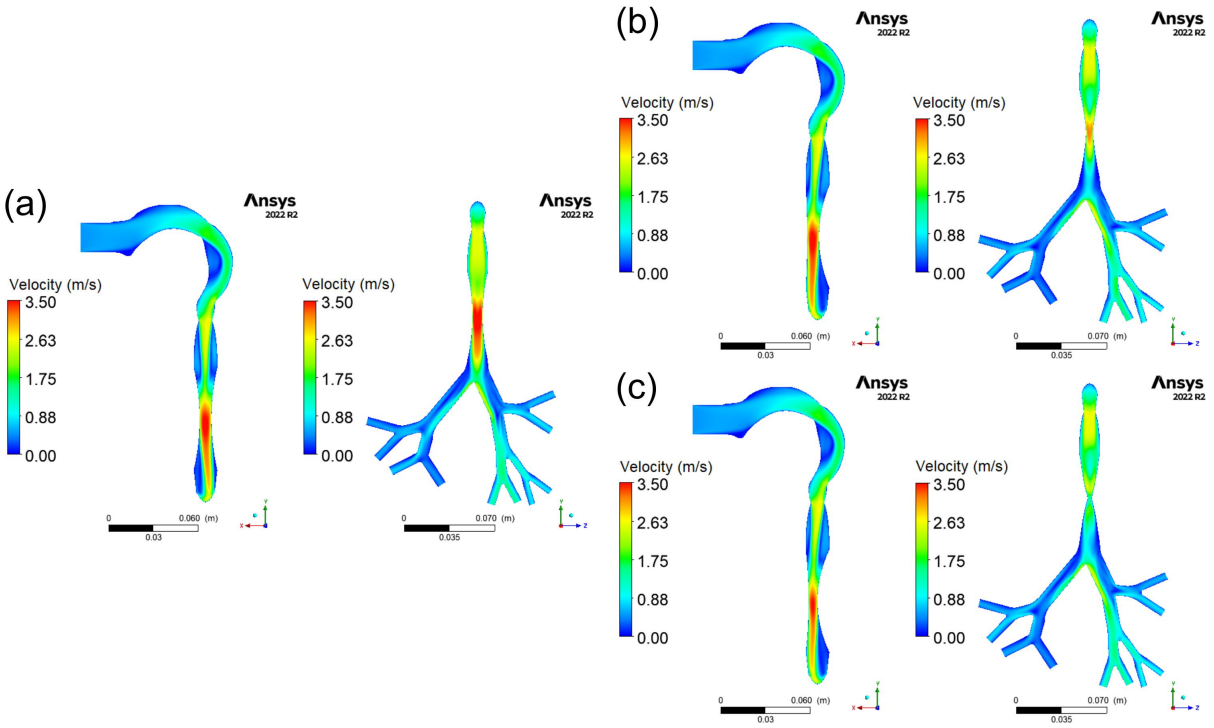

Figure 5.15: *Velocity contours for flow rate of 9 L/min in (a) circular symmetrical, (b) circular asymmetrical and (c) elliptical asymmetrical stenosis.*

Since the flow is skewed to the anterior wall because of the asymmetry of the stenosis, less particles deposit on the carina with respect to the symmetric case. Deposition on the obstruction is not really influenced by the shape of the stenosis at low flow rates. Bigger particles show significant deposition in the right lobes with respect to the healthy scenario and the symmetric stenosis model. The accelerated flow transmits higher momentum to the particles that impact on lower bifurcations.

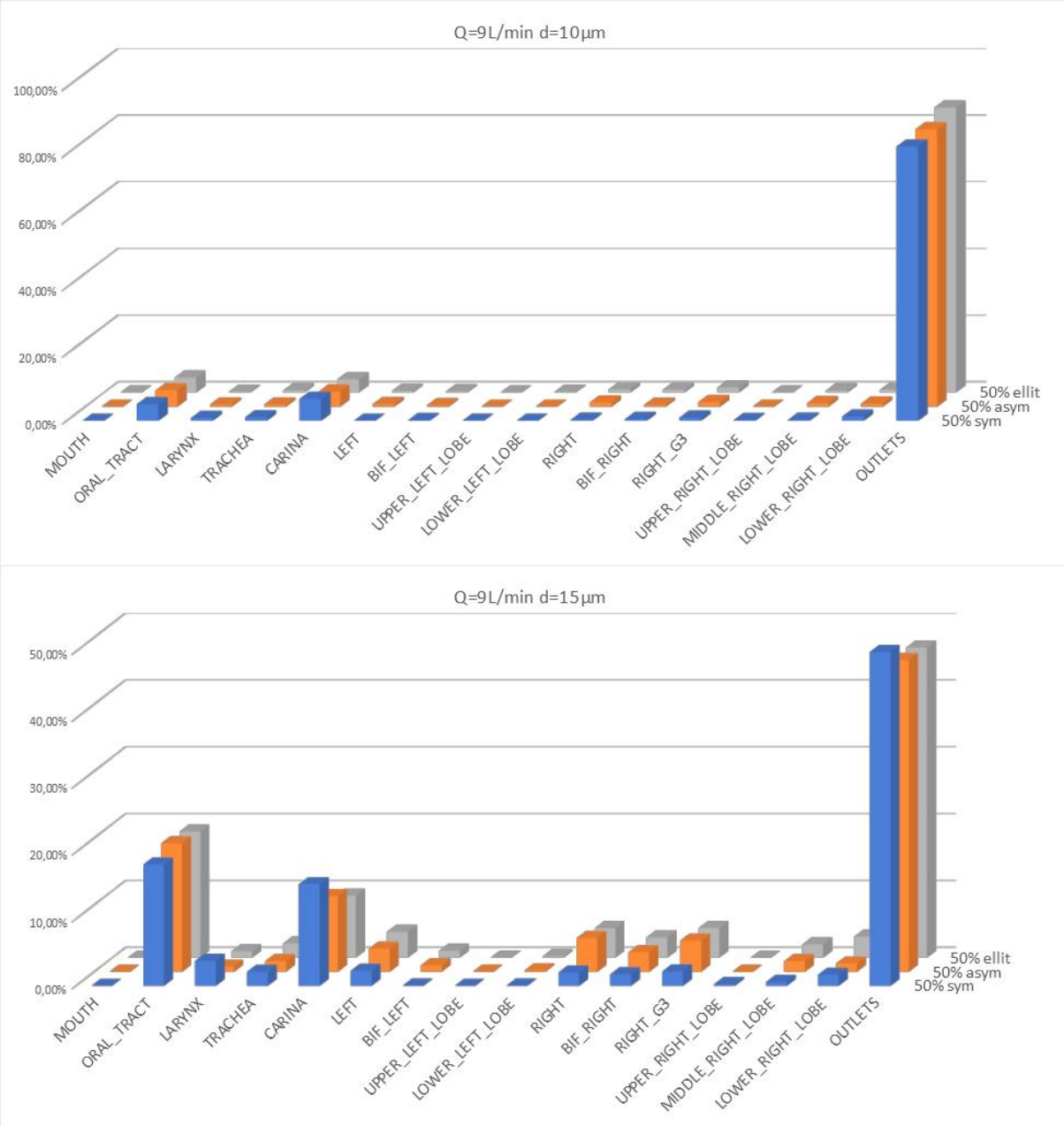

Figure 5.16: *Comparison of deposition fraction in the stenotic airways with different type of stenosis for flow rate of 9 L/min and particle sizes of 10 and 15 µm*

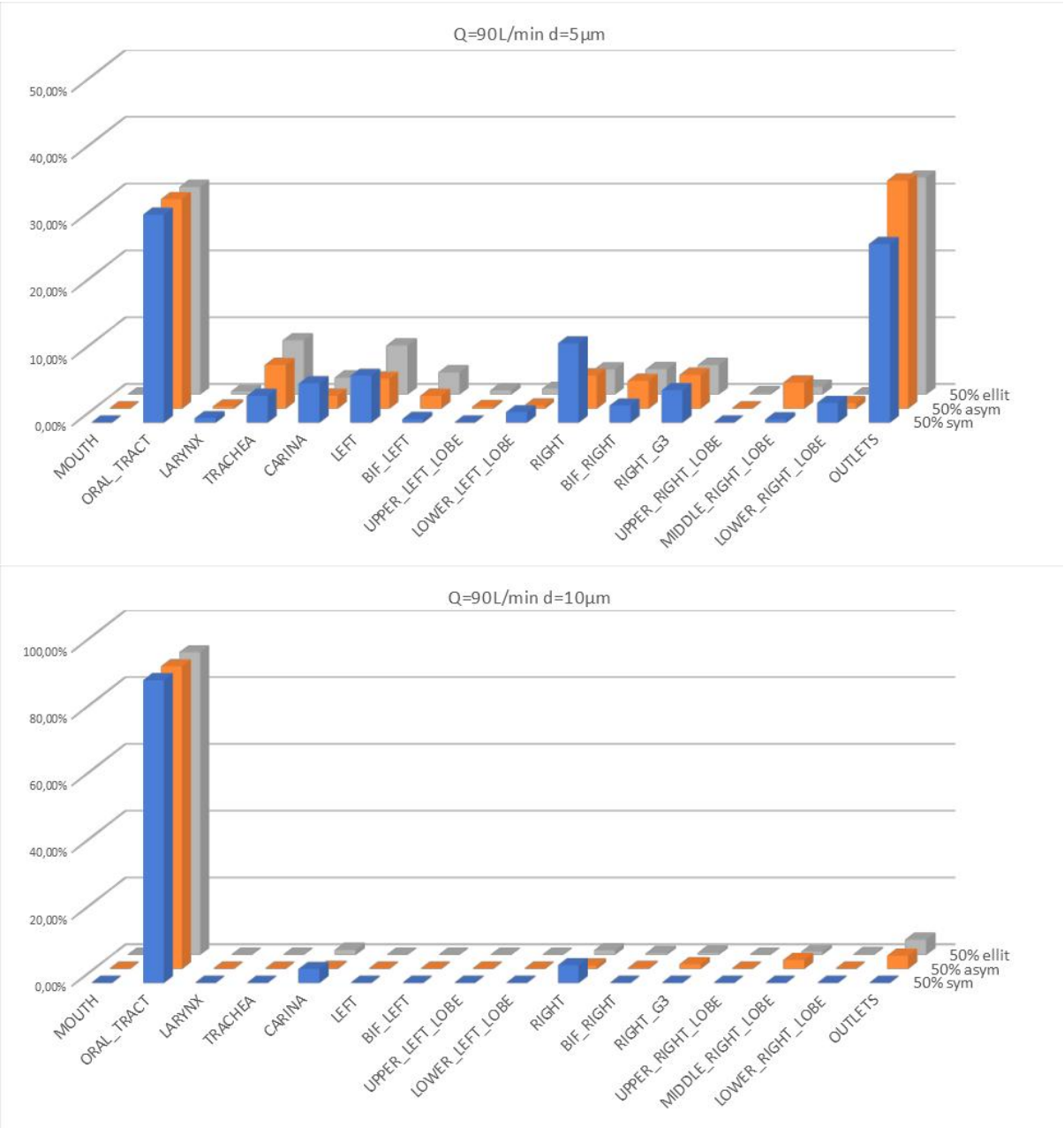

Figure 5.17: *Comparison of deposition fraction in the stenotic airways for different type of stenosis for flow rate of 90 L/min and particle sizes of 5 and 10 µm*

In order to evaluate differences in particle deposition at forced inspiration flow rate, the data from 5 and 10 μm particles have been taken into account, since for smaller and bigger particles there are no differences between the three models under analysis. From the histograms in *Figure 5.17* it is evident that deposition on the obstructed trachea is higher in asymmetric models, because more particles impact and get trapped on the surface where the flow bounces before entering the obstructed section of the trachea (*Figure 5.18*).

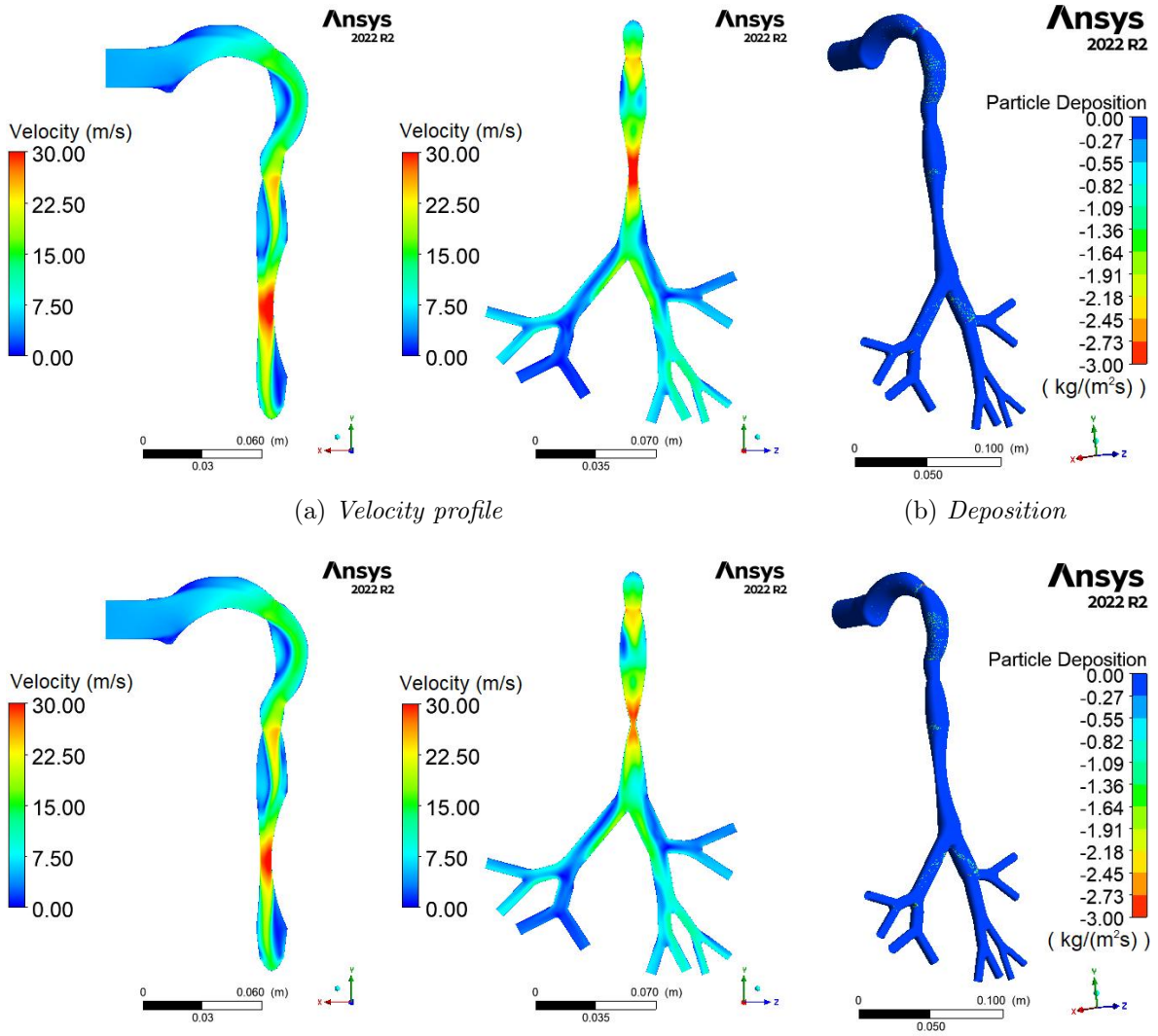

(a) *Velocity profile* (b) *Deposition*

(c) *Velocity profile* (d) *Deposition*

Figure 5.18: *Velocity contours at a flow rate of 90 L/min and 5 µm particle deposition in asymmetric circular (a, b) and asymmetric elliptical (c, d) stenotic model.*

As conclusion of this analysis it can be stated that about 95% of $1\mu m$ particles can reach deeper lung regions under all breathing conditions at different degrees of stenotic trachea. $5\mu m$ particles exit the stenotic models through the outlets for light or normal breathing conditions but have a significant DF around carinal ridges and in the right bronchus. Bigger particles tend to deposit mainly on the upper part of the airways and can reach deeper lung regions only with slow inspiration with a percentage around 80-90% for $10\mu m$ particles, depending on the degree of stenosis, and 50% for $15\mu m$ ones in the worst case of the obstruction.

5.3 Stented airways

The implant of a stent can solve serious obstruction of airways, but at the same time they reduce the inner lumen of the trachea and modify the airflow. Moreover it causes inflammation and other tissue reactions. Therefore it is crucial to investigate the effect of the stent on airflow and particle transport and deposition, both to improve aerosol drug therapies to treat these collateral effect and to avoid worsening of the situation due to deposition of toxic particulate.

5.3.1 Dumon stent

Simulations have shown a slight difference in particle deposition of 1-4% on the Dumon stent for the two different sizes of the device, depending on the particle diameters, as expected from the insertion of a thicker stent. This seems to affect mainly the percentage of particles that can reach deeper lung region with respect to deposition on other surfaces of the model. For this reason the discussion of results will be done on the model with a 1.5mm Dumon stent, keeping in mind that same conclusion can be deduced from the other model with a slight difference.

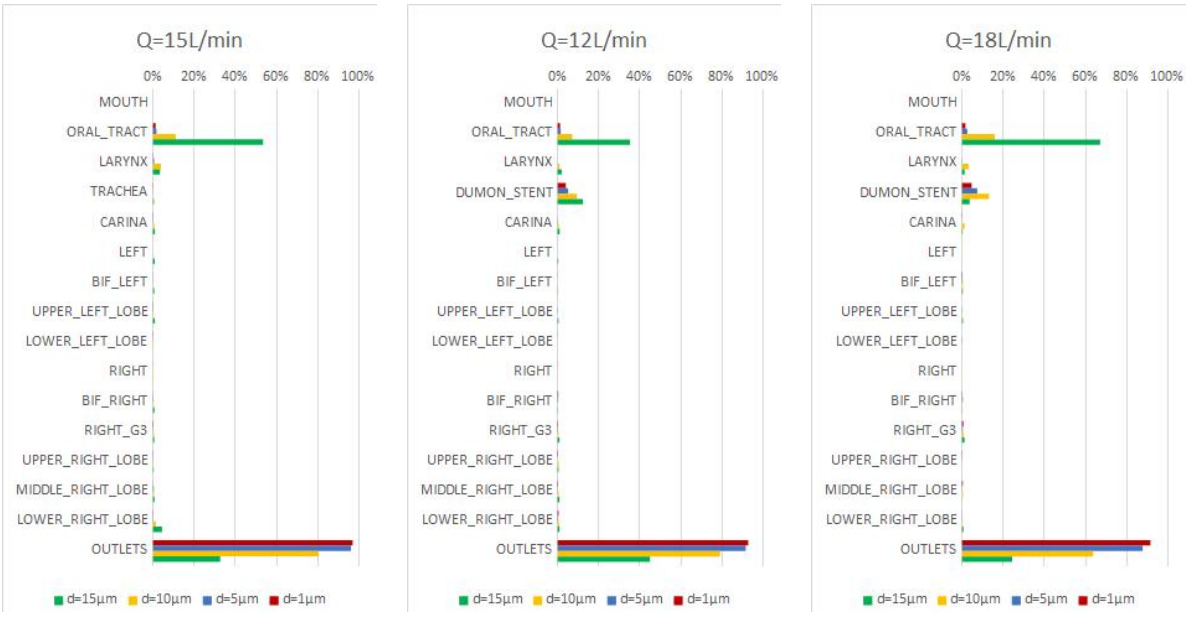

(a) *Healthy model* (b) *Stented model* (c) *Stented model*

Figure 5.19: *Deposition factors in the different regions of the airways for (a) healthy model under light breathing conditions, (b) stented model under light breathing conditions, (c) stented model under normal breathing conditions.*

Deposition on oral tract is not affected by the presence of the prosthetic device and so it depends on flow rate and particle size. A significant DF can be noticed on the surface of the stent, between 5 and 12% depending on particle size. In the case of a entering flow rate of 18 L/min, deposition of larger particles is quite high on the oral tract and this result in a lower deposition on the stent. This confirms the importance of considering the initial oral tract in simulation to give a correct overview of fluid and particle dynamics. From *Figure 5.20* deposition on the upper border of the stent can be noted. In particular the difference between deposition of $15\mu m$ particles on the pharynx and the stent under the two different breathing conditions is evident.
With respect to the healthy case, under normal breathing conditions, the presence of the stent does not affect deposition on other regions of the tracheobronchial tree, but it limits the number of particles that exit the outlets.

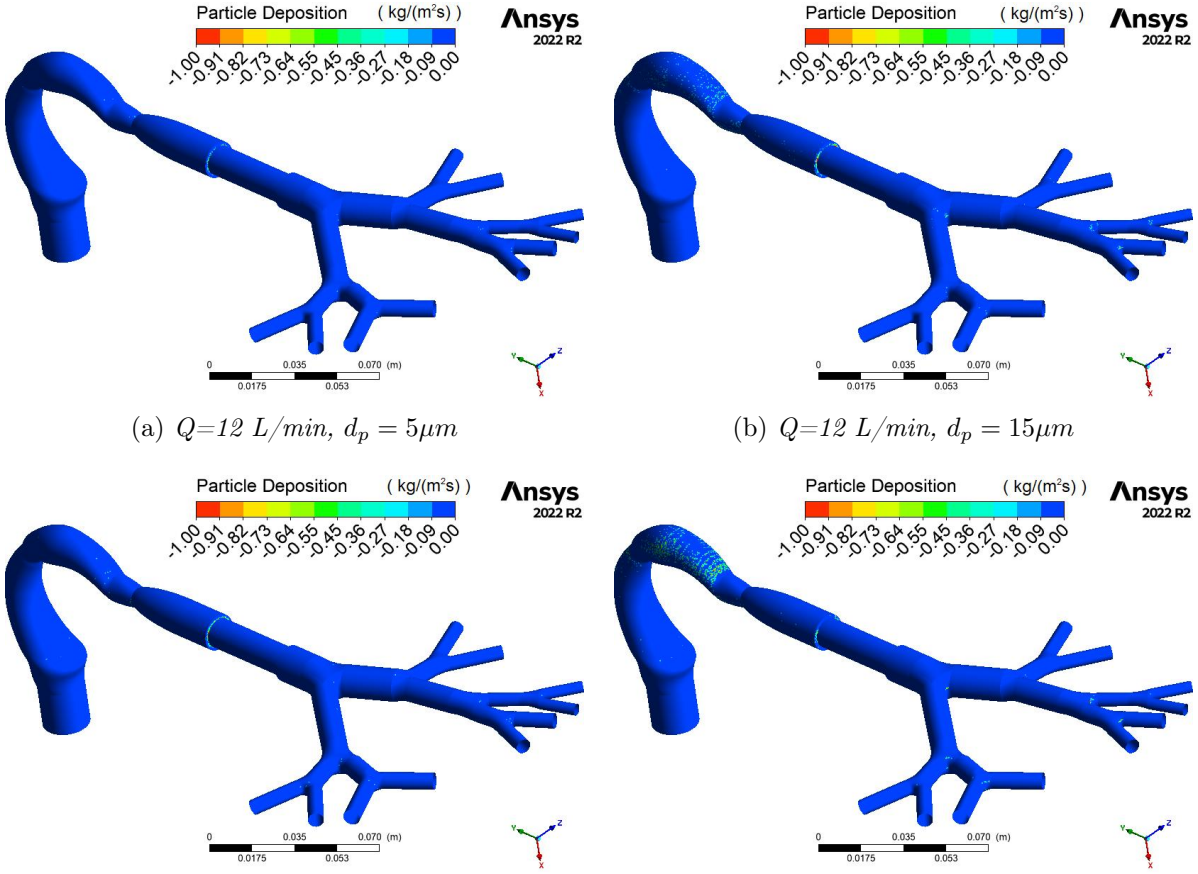

(a) *Q=12 L/min,* $d_p = 5\mu m$

(b) *Q=12 L/min,* $d_p = 15\mu m$

(c) *Q=18 L/min,* $d_p = 5\mu m$

(d) *Q=18 L/min,* $d_p = 15\mu m$

Figure 5.20: *Deposition of particles in the model with Dumon stent of 1.5mm thickness.*

Since guidelines for assumption of lots of drug aerosol are fast and deep inspiration, analysis of airflow and particle transport under forced inspiration flow rates is useful to assess drug distribution in the lungs. Inspiration rate during spirometry test of a patient

that underwent surgery to implant an airway stent has been measured of 3 L/s. In this scenario the fluid flow is more deflected to the posterior and right wall of the stent but tend to divide quite equally at the carina.

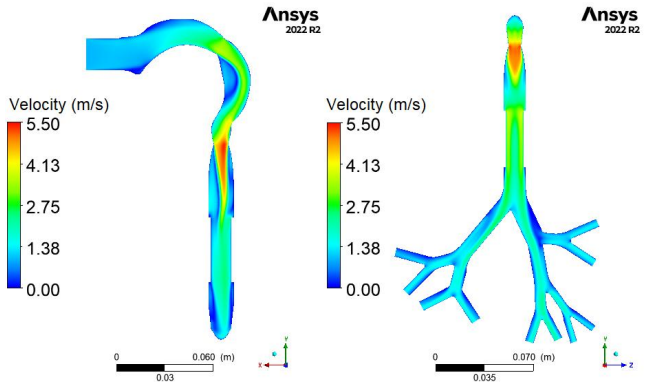

(a) *Velocity profile at Q=18 L/min*

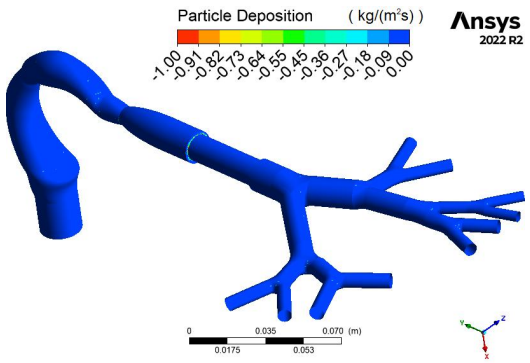

(b) *Deposition of 5μm particles at Q=18 L/min*

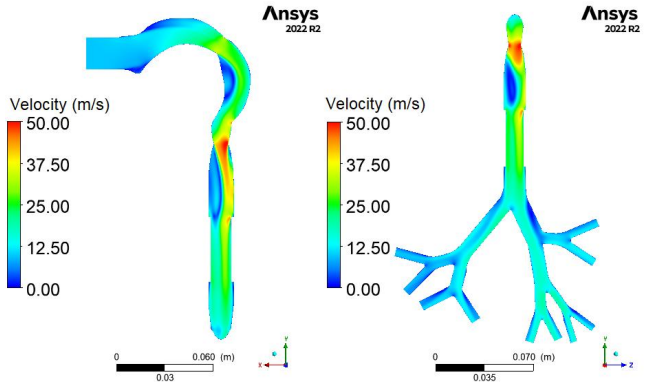

(c) *Velocity profile at Q=180 L/min*

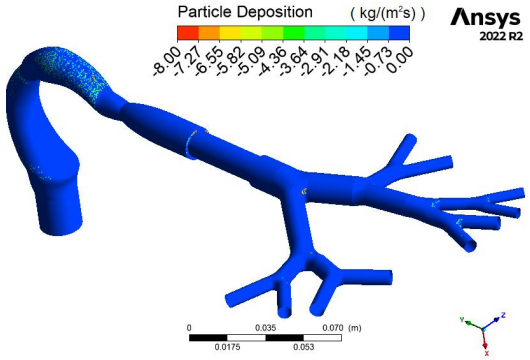

(d) *Deposition of 5μm particles at Q=180 L/min*

Figure 5.21: *Comparison of fluid flow and particles deposition under normal breathing conditions (a, b) and forced inspiration (c, d).*

At such high flow rate, bigger particles deposit at the pharyngeal level, and just few of them reach the tracheobronchial tree and impact on bifurcations in the right lobe before they could reach deeper regions. A small but significant percentage of 5μm particles (5%) deposit on the stent and in different bifurcation at lower levels; just a quarter of the initial number can exit the model through the outlets. The higher percentage of particles reaching deeper lungs region is the 90% of 1μm particles; some of them deposit also on the stent (6%) but the majority exits the model.

5.3.2 Y stent

As for the Dumon stent, the results of the model with tracheobronchial Y stent are presented just for the device with 1.5mm thickness because the general trend in particle transport and deposition is the same, with slightly different DF in the stented region and percentage of exiting particles.

In *Figure 5.23* the deposition factors in the healthy and stented model are compared through the support of histograms and graphical representation of deposition for $10\mu m$ particles. From both representation it is evident that the presence of the stent enhances deposition at the trachea level where the device is implanted, at the carinal ridge and in the subsequent bifurcations, especially in the right lobe. As in the case of the Dumon stent, low DF on the stent for $15\mu m$ particles at flow rate of 18 L/min is due to the high deposition on the oral tract.

Velocity contours in *Figure 5.22* for inlet flow rates of 18 and 180 L/min show a slightly higher flow in the right lobes where the airflow is less deflected: this can explain the higher deposition in bifurcations of the right bronchus.

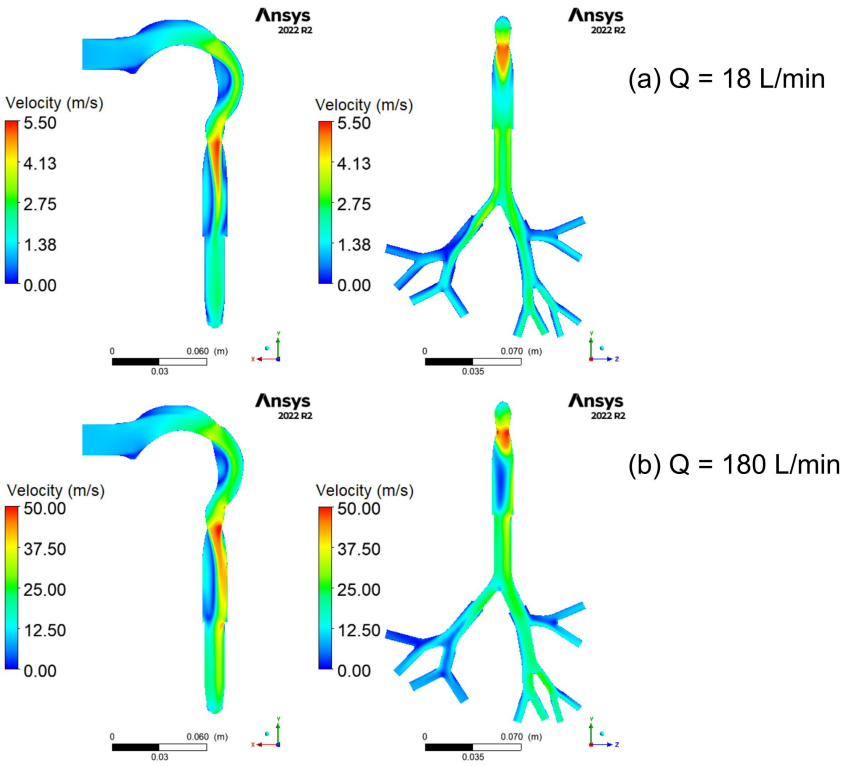

Figure 5.22: *Velocity contours of airflow in the stented model under (a) normal and (b) forced breathing conditions.*

Under forced inspiration flow rate, the division of the flow at the carina is more evident (*Figure 5.22 (b)*). This result in higher deposition of $5\mu m$ particles in the right lobes.

Only 23% of those particles can reach the outlet; bigger particles, as in the other cases, deposit on the oral tract. Only the smallest particles in this analysis can reach deeper lung regions in high concentrations (90%), even if there is a non-null deposition both on the stent and on the bifurcations of the right bronchus (*Figure 5.24*).

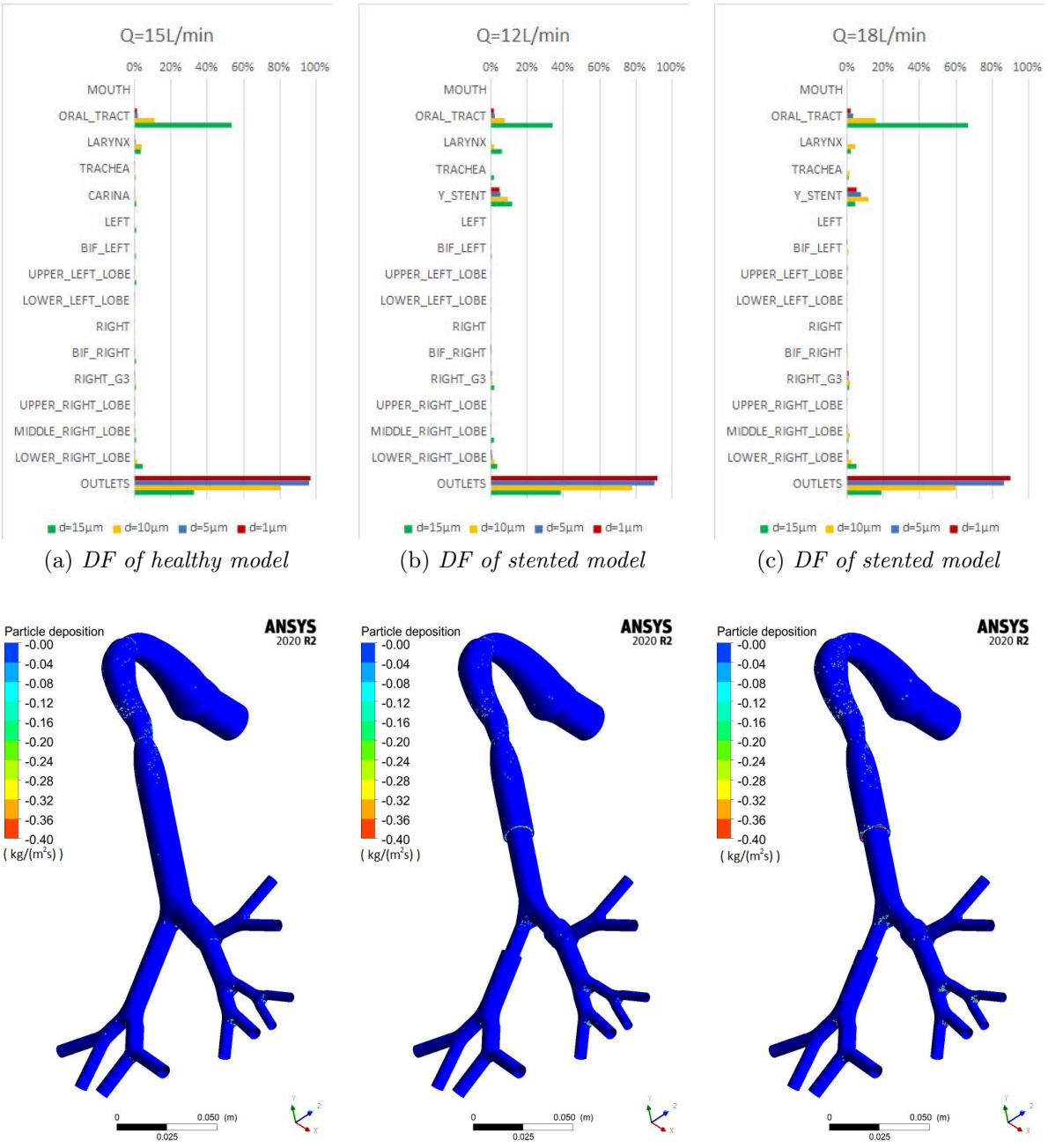

(a) *DF of healthy model* (b) *DF of stented model* (c) *DF of stented model*

(d) *Deposition in healthy model* (e) *Deposition in stented model* (f) *Deposition in stented model*

Figure 5.23: *Deposition factors and graphical representation of 10µm particle deposition in the different regions of the airways for (a, d) healthy model under light breathing conditions, (b, e) stented model under light breathing conditions, (c, f) stented model under normal breathing conditions.*

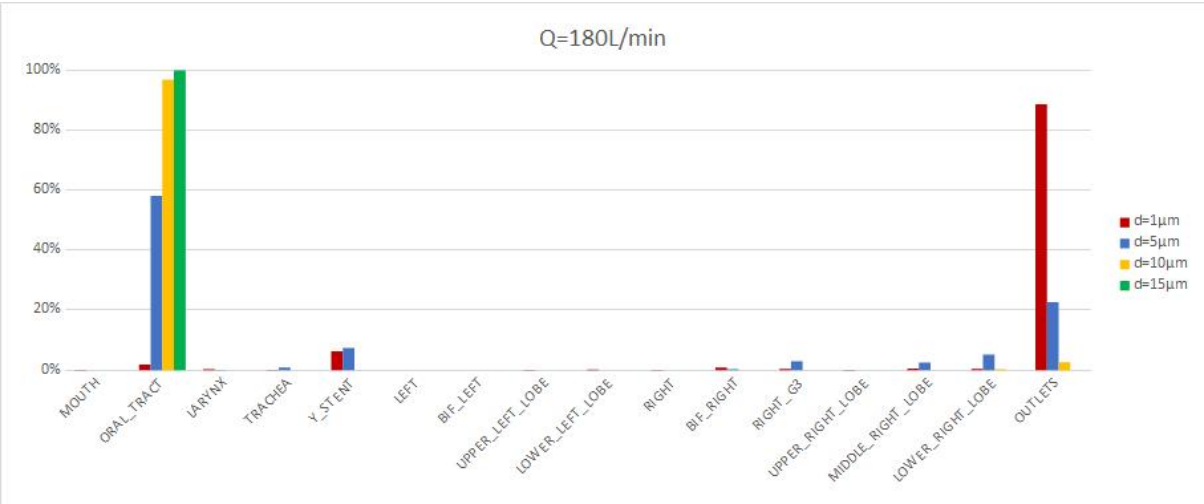

Figure 5.24: *Deposition factors under forced inspiration in the model with the 1.5mm Y stent.*

An interesting comparison can be done between deposition of particles under similar breathing conditions for the model with and without the prosthetic devices.
In *Figure 5.26* the three models are compared. For bigger particles the higher deposition fractions on the oral tract and the larynx are due to the higher flow rate at the inlet. Deposition on the stents are quite similar, 5% for smaller particles and about 9% for the ones with diameter d=10μm. The percentages of particles reaching deeper lung regions are almost the same for all the models.
Figure 5.25 shows deposition fractions on the different stents, confirming the same trend with a slight difference of 2-3% for different thickness at all particle sizes.

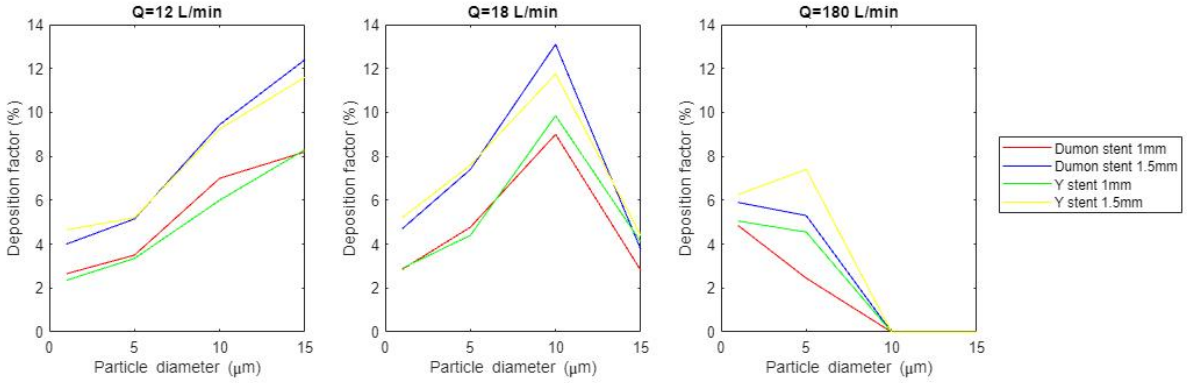

Figure 5.25: *Comparison between deposition fractions of the stents under different breathing conditions.*

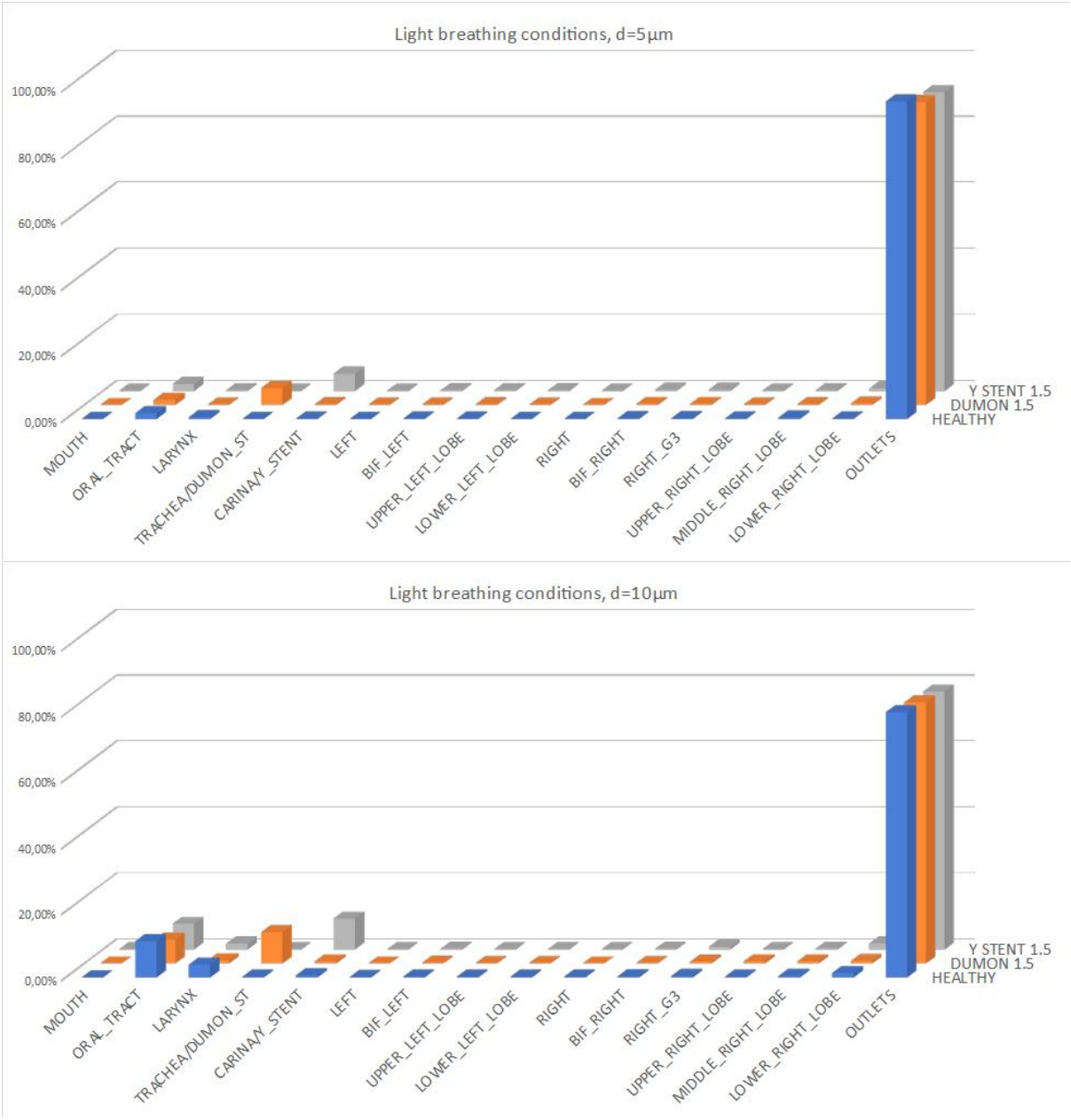

Figure 5.26: *Comparison between DF in healthy and stented models under light breathing conditions (15 L/min for healthy model and 12 L/min for stented models) for 5 and 10 µm particles.*

Chapter 6

Conclusions

The aim of the present work is the evaluation of particle transport and deposition under different conditions of the airway model. Particular attention has been given to stenotic and stented models because there are few studies in literature under realistic breathing conditions. In fact, it is well-known that breathing conditions change a lot in case of obstruction; in worst cases a surgical intervention is needed. In addition, after surgery, breathing rate won't be totally recovered, as spirometry test have shown ([26]). Moreover, since chronic obstructive pulmonary disease is the third leading cause of death worldwide, it is clear that studying airflow and particles dynamics in pre- and post-operatory condition is quite important.
On one side toxic particles deposition can enhance inflammations and promote obstruction, on the other hand the presence of a prosthetic device modifies the inner lumen of the airways and makes the surrounding tissue reacts to the foreign body. In both these situations evaluating particle deposition becomes fundamental to prevent the development of worst side effects and to improve drug aerosol delivery, avoiding overdosing.
Considering the models with stenotic trachea, the results show a significantly increased deposition in the obstructed region, on the subsequent bifurcation and in the first generations of the model for bigger particles with respect to the healthy case. In general data show that deposition tends to increase both with the degree of the stenosis and particle size on the tracheal and carinal surfaces. The comparison has been done considering a flow rate corresponding to light/normal breathing conditions for a healthy and stenotic person. As regard the percentage of small particles (1-5μm) reaching deeper lung regions, it does not seems to be affected by the stenosis at physiologic flow rates. On the contrary, in case of forced inspiration the majority of bigger particles deposits on the oral tract before even reaching the obstructed region, while small particles have different fates: 1μm particles exit the outlet in high concentrations (93-95%) and deposit a little on the bifurcations of the right bronchus, 5μm particles tend to deposit quite uniformly

on the tracheobronchial tree, with higher percentages on the right branch.
Shifting the attention on stented models, the deposition on the two types of stent is quite remarkable: around 3-7% for smaller particles at both flow rates of 12 L/min and 18 L/min (considered as light and normal breathing conditions for a patient who underwent surgery), up to 9-13% for bigger one. $15\mu m$ particles still tend to deposit on the pharynx, reaching deeper lung regions in percentage around 45% and 20-25% at flow rates of 12 L/min and 18 L/min respectively, as in the healthy case. Under forced inspiration just the smallest particles can pass and reach in high concentration the outlets; particles with diameter of $5\mu m$ tend to impact both on the oral tract and in the first generations, with a considerable deposition in the right bronchus in the case of implant of a Y stent.
This analysis has been carried out considering only microparticles because nanoparticles tend to reach deeper generations, while the goal of this work was to evaluate particle deposition around obstructed and stented regions to assess the effect of those modifications on particle transport.
With respect to other works, the employment of an asymmetric model with upper airway tract gives a more complete insight on microparticle deposition in stenotic and stented airways, but there are still some limitations. These limitations regard fundamentally the idealized shape of the model and the obstruction, and the assumption of steady state for the flow. Since it has been proven that transient breathing conditions show higher deposition factors and more realistic results, it would be interesting to investigate the airflow and particle deposition under a realistic breathing cycle. Moreover, it could be interesting to study the airflow and particle dynamics considering the deformability of the upper airways.
Nevertheless, the results of this study may help improving drug aerosol therapy and assessing health risk due to toxic particulate on already weak patients.

Bibliography

[1] ANSYS©. ANSYS CFX-Solver Theory Guide. Release 2020 R1. Jan. 2020.

[2] Bos A. C., Van Holsbeke C., De Backer J. W., Van Westreenen M., Janssens H. M., Vos W. G., Tiddens H. A. W. M., "Patient-Specific Modeling of Regional Antibiotic Concentration Levels in Airways of Patients with Cystic Fibrosis: Are We Dosing High Enough?", *PLoS ONE*, vol. 10, no. 3, Article ID e0118454, 2015.

[3] Brouns M., Jayaraju S. T., Lacor C., De Mey J., Noppen M., Vincken W., Verbanck S., "Tracheal Stenosis: a fluid dynamics study", *Journal of Applied Physiology*, vol. 102, pp. 1178-1184, 2007.

[4] Cai F. S., Yu C. P., "Inertial and interceptial deposition of spherical particles and fibers in a bifurcating airway", *Journal of Aerosol Science*, vol. 19, no. 6, pp. 679-688, 1988.

[5] Chen X., Feng Y., Zhong W., Sun B., Tao F., "Numerical investigation of particle deposition in a triple bifurcation airway due to gravitational sedimentation and inertial impaction", *Powder technology*, no. 323, pp. 284-293, 2018.

[6] Chen X., Zhong W., Sun B., Jin B., Zhou X., "Study on gas/solid flow in an obstructed pulmonary airway with transient flow based on CFD-DPM approach", *Powder Technology*, no. 217, pp. 252-260, 2012.

[7] Chen X., Zhong W., Zhou X., Jin B., Sun B., "CFD-DEM simulation of particle transport and deposition in pulmonary airway", *Powder Technology*, no. 228, pp. 309-318, 2012.

[8] Cheng Y. S., Zhou Y., Chen B. T., "Particle Deposition in a Cast of Human Oral Airways", *Aerosol Science and Technology*, vol. 31, pp. 286-300, 1999.

[9] Comer J. K., Kleinstreuer C., Hyun S., Kim C. S., "Aerosol transport and deposition in sequentially bifurcating airways", *Journal of Biomechanical Engineering Transactions ASME*, no. 122 (2), pp. 152-158, 2000.

[10] Comer J. K., Kleinstreuer C., Zhang Z., "Flow structures and particle deposition patterns in double-bifurcation airway models. Part 1. Air flow fields", *Journal of Fluid Mechanics*, no. 435, pp. 25-54, 2001.

[11] Comer J. K., Kleinstreuer C., Kim C. S., "Flow structures and particle deposition patterns in double-bifurcation airway models. Part 2. Aerosol transport and deposition", *Journal of Fluid Mechanics*, no. 435, pp. 55-80, 2001.

[12] De Backer J. W., Vos W. G., Vinchurkar S. C. et al., "Validation of computational fluid dynamics in CT-based airway models with SPECT/CT", *Radiology*, vol. 257, no. 3, pp. 854-862, 2010.

[13] De Rochefort L., Vial L., Fodil R. et al., "In vitro validation of computational fluid dynamics simulation in human proximal airways with hyperpolarized 3He magnetic resonance phase-contrast velocimetry", *Journal of Applied Physiology*, vol 102, no.5, pp. 2012-2023, 2007.

[14] Dutau H., Musani A.I., Laroumagne S., et al., "Biodegradable Airway Stents - Bench to Bedside: A Comprehensive Review.", *Respiration*, no. 90, pp. 512-521, 2015.

[15] Farkas A., Balásházy I., "Simulation of the effect of local obstructions and blockage on airflow and aerosol deposition in central human airways". *Aerosol Science*, vol. 38, pp. 865-884, 2007.

[16] Farkhadnia F., Gorji T. B., Gorji-Bandpy M., "Airflow, transport and regional deposition of aerosol particles during chronic bronchitis of human central airways", *Australasian College of Physical Scientists and Engineers in Medicine*, no. 39, pp. 43-58, 2016.

[17] Folch E., Keyes C., "Airways stents", *Annals of Cardiothoracic Surgery*, vol. 7, no. 2, pp 273-283, 2018.

[18] Freitag L., Gördes M., Zarogoulidis P., et al., "Towards Individualized Tracheobronchial Stents: Technical, Practical and Legal Considerations.", *Respiration*, no. 94, pp. 442-456, 2017.

[19] Hogg J.C., Timens W., "The Pathology of Chronic Obstructive Pulmonary Disease", *Annual Review of Pathology: Mechanisms of Disease*, vol. 4, pp. 435-459, 2009.

[20] Huang J., Zhang L., Yu S., "Modeling micro-particle deposition in human upper respiratory tract under steady inhalation", *Particuology*, no. 9, pp. 39-43, 2011.

[21] Huang J., Zhang L., "Numerical simulation of micro-particle deposition in a realistic human upper respiratory tract model during transient breathing cycle", *Particuology*, no. 9, pp. 424-431, 2011.

[22] Kleinstreuer C., Zhang Z., Li Z., "Modeling airflow and particle transport/deposition in pulmonary airways", *Respiratory Physiology & Neurobiology*, vol. 163, pp. 128-138, 2008.

[23] Kleinstreuer C., Zhang Z., "Airflow and Particle Transport in the Human Respiratory System", *Annual Review of Fluid Mechanics*, vol. 42, pp. 301-334, 2010.

[24] Li C., Jiang J., Dong H., Zhao K., "Computational modeling and validation of the human nasal airflow under various breathing conditions", *Journal of Biomechanics*, vol. 64, pp. 59-68, 2017.

[25] Luo H. Y., Liu Y., Yang X. L., "Particle deposition in obstructed airways", *Journal of Biomechanics*, vol. 40, pp. 3096-3104, 2007.

[26] Malvè M., Chandra S., López-Villalobos J. L., Finol E. A., Ginel A., Doblaré M., "CFD analysis of the human airways under impedance-based boundary conditions: application to healthy, diseased and stented trachea", *Computer Methods in Biomechanics and Biomedical Engineering*, vol. 16, no. 2, pp. 198-216, 2013.

[27] Malvè M., Sánchez-Matás C., López-Villalobos J. L., "Modelling Particle Transport and Deposition in the Human Healthy and Stented Tracheobronchial Airways", *Annals of Biomedical Engineering*, vol. 48, no. 6, pp. 1805-1820, 2020.

[28] Mylavarapu G., Murugappan S., Mihaescu M., Kalra M., Khosla S., Gutmark E., "Validation of computational fluid dynamics methodology used for human upper airway flow simulations", *Journal of Biomechanics*, vol. 42, no. 10, pp. 1553-1559, 2009.

[29] Nowak N., Kakade P.P., Annapragada A. V., "Computational Fluid Dynamics Simulation of Airflow and Aerosol Deposition in Human Lungs", *Annals of Biomedical Engineering*, vol. 31, pp. 374-390, 2003.

[30] Patwa A., Shah A., "Anatomy and physiology of respiratory system relevant to anaesthesia.", *Indian Journal of Anaesthesia*, vol. 59(9), pp. 533-541, 2015.

[31] Pope R. C. & Dockery D., "Health effects of fine particulate air pollution: lines that connect", *Air repair*, vol. 56, pp. 1368-1380, 2006.

[32] Postma D.S., Bush A., van den Berge M., "Risk factors and early origins of chronic obstructive pulmonary disease", *The Lancet*, vol. 385, pp. 899-909, 2015.

[33] Raaschou-Nielsen O., Andersen Z. J., Beelem R., et al., "Air pollution and lung cancer incidence in 17 European cohorts: prospective analyses from the European Cohorts for Air Pollution Effects (ESCAPE)", *The Lancet Oncology*, vol. 14, no. 9, pp 813-822, 2013.

[34] Rahimi-Gorji M., Gorji T. B., Gorji-Bandpy M., "Details of regional particle deposition and airflow structures in a realistic model of human tracheobronchial airways: two-phase flow simulation", *Computers in Biology and Medicine*, no. 74, pp. 1-17, 2016.

[35] Rahimi-Gorji M., Pourmehran O., Gorji-Bandpy M., Gorji T. B., "CFD simulation of airflow behavior and particle transport and deposition in different breathing conditions through the realistic model of human airways", *Journal of Molecular Liquids*, no. 209, pp. 121-133, 2015.

[36] Schlesinger R. B., Bohning D. E., Chai T. L., Lippman M., "Particle deposition in a hollow cast of the human tracheobronchial tree", *Journal of Aerosol Science*, vol. 8, pp. 429-445, 1977.

[37] Schlichting H., Gersten K., "Boundary-Layer Theory - 9^{th} Edition", *Springer*, 2017.

[38] Segal R. A., Martonen T. B., Kim C. S., Shearer M., "Computer simulations of particle deposition in the lungs of chronic obstructive pulmonary disease patients", *Inhalation Toxicology*, vol. 14 (7), pp. 705-720, 2002.

[39] Snider G.L., Kleinerman J.L., Thurlbeck W.M., Engally Z.H., "Definition of emphysema. Report of the National Heart, Lung, and Blood Institute workshop.", *American Review of Respiratory Disease*, vol. 132, pp. 182-85, 1985.

[40] Sul B., Wallqvist A., Morris M. J., Reifman J., Rakesh V., "A computational study of the respiratory airflow characteristics in normal and obstructed human airways", *Computers in Biology and Medicine*, vol. 52, pp. 130-143, 2014.

[41] Van Scott M.R., Chandler J., Olmstead S., Brown J.M., Mannie M., "Airway Anatomy, Physiology, and Inflammation." in: Meggs W. "The Toxicant Induction of Irritant Asthma, Rhinitis, and Related Conditions.", Springer, Boston, MA, 2013.

[42] Weibel E. R., "Morphometry of the human lung", Academic Press, New York, 1963.

[43] Yamao K., Kitano M., Chiba Y. et al., "Endoscopic placement of covered versus uncovered self-expandable metal stents for palliation of malignant gastric outlet obstruction", *Gut*, no. 70, pp. 1244-1252, 2021.

[44] Yang X. L., Liu Y., Luo H. Y., "Respiratory flow in obstructed airways", *Journal of Biomechanics*, vol. 39, pp. 2743-2751, 2006.

[45] Zhang B., Qi S., Yue Y., Shen J., Li C., Qian W., Wu J., "Particle Disposition in the Realistic Airway Tree Models of Subjects with Tracheal Bronchus and COPD", *BioMed Research International*, vol 2018. Article ID 7428609, 2018.

[46] Zhang Z., Kleinstreuer C., "Low-Reynolds-number turbulent flows in locally constricted conduits: a comparison study", *AIAA Journal*, no. 41, pp. 831-840, 2003.

[47] Zhang Z., Kleinstreuer C., Kim C. S., "Micro-particle transport and deposition in a human oral airway model", *Journal of Aerosol Science*, vol. 33, pp. 1635-1652, 2002.

[48] Zhang Z., Kleinstreuer C., Donohue J. F., Kim C. S., "Comparison of micro- and nano-particle depositions in a human upper airway model", *Journal of Aerosol Science*, vol. 36, pp. 211-233, 2005.

Appendix A

Regional deposition fractions

Table A.1: Regional deposition fractions (in %) in the healthy model.

$d_p = 1\mu m$	Oral airway	Trachea	Carina	Left bronchus	Right bronchus	Outlets
15 L/min	1.50	0.20	0.15	0.40	0.75	96.95
30 L/min	2.50	0	0.15	0.45	1.05	95.85
60 L/min	2.25	0.15	0.10	0.55	1.15	95.80
$d_p = 5\mu m$	Oral airway	Trachea	Carina	Left bronchus	Right bronchus	Outlets
15 L/min	2.25	0.05	0.15	0.30	1.10	96.15
30 L/min	4.25	0.20	0.30	0.40	1.80	93.05
60 L/min	14.60	0.25	0.75	1.65	1.90	80.85
$d_p = 10\mu m$	Oral airway	Trachea	Carina	Left bronchus	Right bronchus	Outlets
15 L/min	14.85	0.20	0.75	0.80	3.05	80.45
30 L/min	46.45	0.75	2.60	10.05	5.25	34.5
60 L/min	80.55	0	1.25	7.70	1.35	9.15
$d_p = 15\mu m$	Oral airway	Trachea	Carina	Left bronchus	Right bronchus	Outlets
15 L/min	56.80	0.45	0.90	2.45	6.75	32.65
30 L/min	79.00	0	8.95	8.80	3.20	0.05
60 L/min	96.00	0	0	0	1.70	2.30

Table A.2: Regional deposition fractions (in %) in the stenotic models at flow rate of 6 L/min.

$d_p = 1\mu m$	Oral airway	Trachea	Carina	Left bronchus	Right bronchus	Outlets
20%	1.30	0.10	0.35	0.25	1.25	96.65
30%	1.55	0.10	0.35	0.35	0.80	96.75
50%	1.45	0.20	0.40	0.35	1.40	96.05
50% asym	1.60	0.25	0.50	0.30	2.10	95.20
50% ellit	1.30	0.35	0.60	0.25	1.35	96.00
$d_p = 5\mu m$	Oral airway	Trachea	Carina	Left bronchus	Right bronchus	Outlets
20%	1.70	0.50	0.40	0.20	1.10	96.30
30%	1.65	0.20	0.45	0.20	1.20	96.20
50%	1.50	0.25	0.75	0.15	1.35	95.80
50% asym	1.60	0.25	0.50	0.30	2.10	95.20
50% ellit	1.55	0.35	0.55	0.35	1.80	95.20
$d_p = 10\mu m$	Oral airway	Trachea	Carina	Left bronchus	Right bronchus	Outlets
20%	2.75	0.05	0.40	0.60	1.35	94.80
30%	2.65	0.25	0.90	0.10	2.30	93.75
50%	2.25	0.55	2.45	0.25	1.95	92.55
50% asym	2.95	0.25	2.20	0.35	3.35	90.85
50% ellit	2.60	0.25	2.00	0.80	2.40	92.00
$d_p = 15\mu m$	Oral airway	Trachea	Carina	Left bronchus	Right bronchus	Outlets
20%	6.75	0	2.25	0.60	2.20	88.20
30%	7.05	0.35	3.45	0.50	3.50	85.05
50%	6.25	1.40	7.20	0.65	5.45	92.55
50% asym	7.30	0.80	7.80	1.85	11.40	70.75
50% ellit	7.50	0.70	7.60	2.65	8.55	72.95

Table A.3: Regional deposition fractions (in %) in the stenotic models at flow rate of 9 L/min.

$d_p = 1\mu m$	Oral airway	Trachea	Carina	Left bronchus	Right bronchus	Outlets
20%	1.35	0.50	0.40	0.45	0.75	97.00
30%	1.50	0.15	0.20	0.35	1.50	96.25
50%	1.60	0.15	0.45	0.15	1.10	96.50
50% asym	1.70	0.25	0.40	0.20	1.55	95.90
50% ellit	1.45	0.10	0.40	0.30	1.20	96.50
$d_p = 5\mu m$	Oral airway	Trachea	Carina	Left bronchus	Right bronchus	Outlets
20%	2.00	0	0.25	0.50	1.25	96.00
30%	1.90	0.05	0.20	0.35	0.90	96.60
50%	1.80	0.30	0.75	0.15	1.95	95.05
50% asym	3.35	0.40	0.50	0.20	2.35	94.20
50% ellit	1.80	0.10	0.70	0.35	1.60	95.45
$d_p = 10\mu m$	Oral airway	Trachea	Carina	Left bronchus	Right bronchus	Outlets
20%	4.95	0.20	0.90	0.75	2.10	91.10
30%	6.45	0.30	2.00	0.40	2.05	88.75
50%	5.85	1.10	6.60	0.30	3.85	82.30
50% asym	5.55	0.60	4.50	1.15	5.00	83.20
50% ellit	4.65	0.60	3.90	0.85	4.60	85.40
$d_p = 15\mu m$	Oral airway	Trachea	Carina	Left bronchus	Right bronchus	Outlets
20%	20.25	1.80	2.15	1.20	4.25	70.30
30%	21.75	1.30	5.05	1.20	3.15	67.05
50%	21.90	2.10	15.20	2.35	8.35	49.95
50% asym	19.95	1.60	11.35	4.60	15.45	46.65
50% ellit	19.80	2.15	9.30	5.25	17.05	46.40

Table A.4: Regional deposition fractions (in %) in the stenotic models at flow rate of 90 L/min.

$d_p = 1\mu m$	Oral airway	Trachea	Carina	Left bronchus	Right bronchus	Outlets
20%	2.05	0.10	0.40	0.30	1.50	95.55
30%	2.75	0.45	0.40	0.55	1.35	94.45
50%	3.00	0.70	0.65	0.20	1.75	93.50
50% asym	2.30	0.35	0.60	0.40	2.00	94.25
50% ellit	2.35	0.50	0.50	0.45	1.40	94.70
$d_p = 5\mu m$	Oral airway	Trachea	Carina	Left bronchus	Right bronchus	Outlets
20%	30.90	2.60	2.75	6.90	9.30	47.55
30%	33.30	0.45	4.65	5.25	6.95	49.40
50%	31.75	4.00	5.85	9.05	22.65	26.70
50% asym	31.65	6.50	1.90	6.05	18.80	34.10
50% ellit	31.50	8.10	2.50	12.10	13.35	32.45
$d_p = 10\mu m$	Oral airway	Trachea	Carina	Left bronchus	Right bronchus	Outlets
20%	90.00	0	0.60	2.40	6.75	0.25
30%	89.80	0	4.20	6.00	0	0
50%	90.55	0	4.15	0	5.30	0
50% asym	90.55	0	0.25	0	5.25	3.95
50% ellit	90.50	0	1.45	0	3.55	4.50
$d_p = 15\mu m$	Oral airway	Trachea	Carina	Left bronchus	Right bronchus	Outlets
20%	100	0	0	0	0	0
30%	100	0	0	0	0	0
50%	100	0	0	0	0	0
50% asym	100	0	0	0	0	0
50% ellit	100	0	0	0	0	0

Table A.5: Regional deposition fractions (in %) in the stented models at flow rate of 12 L/min.

$d_p = 1\mu m$	Oral airway	Trachea	Stent	Carina	Left bronchus	Right bronchus	Outlets
Dumon st. 1mm	1.70	/	2.65	0.25	0.50	1.05	93.70
Dumon st. 1.5mm	1.20	/	4.00	0	0.30	1.65	92.85
Y stent 1 mm	1.55	0	2.35	/	0.25	1.50	94.35
Y stent 1.5mm	1.65	0	4.65	/	0.15	1.40	92.10
$d_p = 5\mu m$	Oral airway	Trachea	Stent	Carina	Left bronchus	Right bronchus	Outlets
Dumon st. 1mm	2.00	/	3.50	0.20	0.30	1.20	92.80
Dumon st. 1.5mm	1.60	/	5.15	0.15	0.35	1.15	91.60
Y stent 1 mm	2.00	0	3.35	/	0.50	0.95	93.15
Y stent 1.5mm	2.25	0	5.20	/	0.55	1.55	90.40
$d_p = 10\mu m$	Oral airway	Trachea	Stent	Carina	Left bronchus	Right bronchus	Outlets
Dumon st. 1mm	7.65	/	7.00	0.25	0.50	2.60	82.00
Dumon st. 1.5mm	8.10	/	9.45	0.60	0.35	2.35	79.15
Y stent 1 mm	8.85	0.15	6.00	/	0.55	2.50	81.95
Y stent 1.5mm	9.40	0.05	9.25	/	0.25	2.90	78.10
$d_p = 15\mu m$	Oral airway	Trachea	Stent	Carina	Left bronchus	Right bronchus	Outlets
Dumon st. 1mm	38.25	/	8.20	1.05	1.10	2.35	49.05
Dumon st. 1.5mm	37.25	/	12.40	1.00	0.90	3.45	45.00
Y stent 1 mm	39.60	0.2	8.30	/	0.95	5.10	45.85
Y stent 1.5mm	40.15	1.65	11.60	/	0.60	7.40	38.60

Table A.6: Regional deposition fractions (in %) in the stented models at flow rate of 18 L/min.

$d_p = 1\mu m$	Oral airway	Trachea	Stent	Carina	Left bronchus	Right bronchus	Outlets
Dumon stent 1mm	1.70	/	2.85	0.30	0.35	1.15	93.55
Dumon stent 1.5mm	1.70	/	4.70	0.20	0.40	1.45	91.50
Y stent 1 mm	1.90	0.05	2.90	/	0.30	1.30	93.25
Y stent 1.5mm	2.00	0	5.20	/	0.80	1.95	90.05
$d_p = 5\mu m$	Oral airway	Trachea	Stent	Carina	Left bronchus	Right bronchus	Outlets
Dumon stent 1mm	3.25	/	4.70	0.20	0.55	1.35	89.95
Dumon stent 1.5mm	2.75	/	7.40	0.10	0.75	1.25	87.75
Y stent 1 mm	2.95	0	4.40	/	0.70	2.05	89.90
Y stent 1.5mm	3.55	0.05	7.60	/	0.40	1.90	86.50
$d_p = 10\mu m$	Oral airway	Trachea	Stent	Carina	Left bronchus	Right bronchus	Outlets
Dumon stent 1mm	20.20	/	9.00	0.35	1.85	2.60	66.00
Dumon stent 1.5mm	19.15	/	13.10	1.20	0.80	1.95	63.75
Y stent 1 mm	20.35	0.10	9.85	/	0.70	5.30	63.70
Y stent 1.5mm	20.25	1.25	11.75	/	0.90	5.95	59.85
$d_p = 15\mu m$	Oral airway	Trachea	Stent	Carina	Left bronchus	Right bronchus	Outlets
Dumon stent 1mm	68.35	/	2.80	0.25	1.40	3.10	24.05
Dumon stent 1.5mm	68.45	/	3.75	0.35	0.90	2.20	24.35
Y stent 1 mm	69.75	0.25	4.10	/	0.70	5.95	19.25
Y stent 1.5mm	68.65	0.70	4.40	/	0.55	6.85	18.85

Table A.7: Regional deposition fractions (in %) in the stented models at flow rate of 180 L/min.

$d_p = 1\mu m$	Oral airway	Trachea	Stent	Carina	Left bronchus	Right bronchus	Outlets
Dumon stent 1mm	2.95	/	4.85	0.40	0.75	0.80	90.20
Dumon stent 1.5mm	2.05	/	5.90	0.40	0.70	1.25	89.70
Y stent 1 mm	3.10	0	5.05	/	0.15	2.55	89.15
Y stent 1.5mm	2.15	0.10	6.25	/	0.25	2.40	88.70
$d_p = 5\mu m$	Oral airway	Trachea	Stent	Carina	Left bronchus	Right bronchus	Outlets
Dumon stent 1mm	59.25	/	2.45	2.15	3.20	3	29.95
Dumon stent 1.5mm	58.00	/	5.35	3.20	1.95	7.1	23.85
Y stent 1 mm	59.00	0.30	4.55	/	0	18.40	17.75
Y stent 1.5mm	58.20	0.80	7.40	/	0	10.95	22.65
$d_p = 10\mu m$	Oral airway	Trachea	Stent	Carina	Left bronchus	Right bronchus	Outlets
Dumon stent 1mm	97.35	/	0	0	2.65	0	0
Dumon stent 1.5mm	97.00	/	0	0.30	0	2.50	0
Y stent 1 mm	97.35	0	0	/	0	2.65	0
Y stent 1.5mm	96.90	0	0	/	0	0.30	2.65
$d_p = 15\mu m$	Oral airway	Trachea	Stent	Carina	Left bronchus	Right bronchus	Outlets
Dumon stent 1mm	100	/	0	0	0	0	0
Dumon stent 1.5mm	100	/	0	0	0	0	0
Y stent 1 mm	100	0	0	/	0	0	0
Y stent 1.5mm	100	0	0	/	0	0	0

Appendix B

Turbulence model

Turbulence models have been developed in order to take into account the effects of turbulence without recourse to extremely fine mesh and direct numerical simulation. Most turbulence models are statistical models that consider the variables under analysis as the sum of an average component and a time-varying, fluctuating one. In this way the unsteady Navier-Stokes equations are modified to produce the Reynolds Averaged Navier-Stokes (RANS) equations which represent the mean flow quantities only. The additional variables representing the fluctuating quantities are called "turbulent" or "Reynolds" stresses and are calculated through the additional equations of the turbulence model.

B.1 Reynolds Averaged Navier-Stokes equations

Introducing averaged and fluctuating components, the velocity can be written as:

$$\mathbf{U} = \bar{\mathbf{U}} + \mathbf{u} \tag{B.1}$$

The average component is given by:

$$\bar{\mathbf{U}} = \frac{1}{\Delta t} \int_t^{t+\Delta t} \mathbf{U}\, dt \tag{B.2}$$

where Δt is the time scale, larger with respect to the turbulent fluctuations but smaller than the time scale to which the equations are solved.
Substituting in the original Navier-Stokes equations the RANS system is obtained:

$$\frac{\partial \rho}{\partial t} + \nabla \cdot (\rho\, \bar{\mathbf{U}}) = 0 \tag{B.3}$$

$$\frac{\partial \rho\, \bar{\mathbf{U}}}{\partial t} + \nabla \cdot \left(\rho\, \bar{\mathbf{U}} \otimes \bar{\mathbf{U}}\right) = -\nabla p + \nabla \cdot \left(\tau - \rho\, \overline{\mathbf{u} \otimes \mathbf{u}}\right), + \mathbf{S}_M \tag{B.4}$$

$$\frac{\partial \rho\, h_{tot}}{\partial t} - \frac{\partial p}{\partial t} + \nabla \cdot \left(\rho\, \bar{\mathbf{U}}\, h_{tot}\right) = \nabla \cdot \left(\lambda\, \nabla T - \rho\, \overline{\mathbf{u}\, h}\right) + \nabla \cdot \left(\bar{\mathbf{U}} \cdot \left(\tau - \rho\, \overline{\mathbf{u} \otimes \mathbf{u}}\right)\right) + S_E \quad \text{(B.5)}$$

where τ is the molecular stress tensor, and the Total Enthalpy is given by:

$$h_{tot} = h + \frac{1}{2}\bar{\mathbf{U}}^2 + k \quad \text{(B.6)}$$

where $k = \frac{1}{2}\overline{\mathbf{u}^2}$ is the turbulent kinetic energy.
The terms $\rho\, \overline{\mathbf{u} \otimes \mathbf{u}}$ and $\rho\, \overline{\mathbf{u}\, h}$ are the Reynolds stresses and flux that are computed through turbulence models. CFX statistical models can be divided into eddy viscosity models and Reynolds stress models.
The Eddy Viscosity turbulence models consider turbulence as a set of small eddies which are continuously forming and dissipating. This brings to the assumption of two hypotheses: the eddy viscosity and eddy diffusivity hypotheses. The first states that the Reynolds stress are related to the mean velocity gradients and the eddy viscosity through the relation:

$$-\rho\, \overline{\mathbf{u} \otimes \mathbf{u}} = \mu_t \left(\nabla \bar{\mathbf{U}} + (\nabla \bar{\mathbf{U}})^T\right) - \frac{2}{3}\delta_{ij}\left(\rho\, k + \mu_t\, \nabla \cdot \bar{\mathbf{U}}\right) \quad \text{(B.7)}$$

while the second relate Reynolds fluxes of a scalar to the mean scalar gradient:

$$-\rho\, \overline{\mathbf{u}\, h} = \Gamma_t\, \nabla h \quad \text{(B.8)}$$

μ_t and Γ_t are the eddy viscosity and diffusivity respectively and they are linked together by the Prandtl number: $\Gamma_t = \frac{\mu_t}{Pr_t}$.
Under these hypotheses the momentum and energy conservation equations become:

$$\frac{\partial \rho \bar{\mathbf{U}}}{\partial t} + \nabla \cdot (\rho \bar{\mathbf{U}} \otimes \bar{\mathbf{U}}) = -\nabla p' + \nabla \cdot \left(\mu_{eff}\left(\nabla \bar{\mathbf{U}} + (\nabla \bar{\mathbf{U}})^T\right)\right) + \mathbf{S}_M \quad \text{(B.9)}$$

$$\frac{\partial (\rho h_{tot}}{\partial t} - \frac{\partial p}{\partial t} + \nabla \cdot \left(\rho\, \bar{\mathbf{U}}\, h_{tot}\right) = \nabla \cdot \left(\lambda\, \nabla T + \frac{\mu_t}{Pr_t}\, \nabla h\right) + \nabla \cdot \left(\bar{\mathbf{U}} \cdot (\tau - \rho\, \overline{\mathbf{u} \otimes \mathbf{u}})\right) + S_E \quad \text{(B.10)}$$

where S_M is the sum of body forces, $\mu_{eff} = \mu + \mu_t$ is the Effective Viscosity, p' is the modified pressure defined by $p' = p + \frac{2}{3}\rho k + \frac{2}{3}\mu_{eff} \nabla \cdot \bar{\mathbf{U}}$. Eddy viscosity models are distinguished by the manner in which they calculate eddy viscosity and diffusivity.

B.2 The Wilcox k-ω model

The Wilcox $k-\omega$ model links the eddy viscosity to the turbulent kinetic energy k and the turbulent frequency ω:

$$\mu_t = \rho \frac{k}{\omega} \tag{B.11}$$

The model consists of two transport equation for k and ω:

$$\frac{\partial(\rho k)}{\partial t} + \nabla \cdot (\rho \, \mathbf{U} \, k) = \nabla \cdot \left[\left(\mu + \frac{\mu_t}{\sigma_k} \right) \nabla k \right] + P_k + P_{kb} - \beta' \rho k \omega \tag{B.12}$$

$$\frac{\partial(\rho \omega)}{\partial t} + \nabla \cdot (\rho \, \mathbf{U} \, \omega) = \nabla \cdot \left[\left(\mu + \frac{\mu_t}{\sigma_\omega} \right) \nabla \omega \right] + \alpha \frac{\omega}{k} P_k + P_{\omega b} - \beta \rho \omega^2 \tag{B.13}$$

The model constants are given by:

$$\beta' = 0.09 \tag{B.14}$$

$$\alpha = 5/9 \tag{B.15}$$

$$\beta = 0.075 \tag{B.16}$$

$$\sigma_k = 2 \tag{B.17}$$

$$\sigma_\omega = 2 \tag{B.18}$$

P_k is the production rate of turbulence calculated from:

$$P_k = \mu_t \, \nabla \mathbf{U} \cdot \left(\nabla \mathbf{U} + \nabla \mathbf{U}^T \right) - \frac{2}{3} \nabla \cdot \mathbf{U} \left(3 \mu_t \, \nabla \mathbf{U} + \rho \, k \right) \tag{B.19}$$

For incompressible flow, $\nabla \cdot \mathbf{U}$ is small and the second term on the right side of the equation does not contribute significantly to the production. P_{kb} and $P_{\omega b}$ represent the influence of the buoyancy forces, and are included in the equations only if the "Buoyancy Turbulence" option in CFX is enabled.

B.3 Shear Stress Transport model

The $k-\omega$-based SST model takes into account the transport of turbulent shear stress to avoid overprediction of the eddy viscosity. To do this, it uses a limiter to the formulation of the eddy kinematic viscosity $\nu_t = \frac{\mu_t}{\rho}$:

$$\nu_t = \frac{\alpha_1 \, k}{max(\alpha_1 \omega, \, SF_2)} \tag{B.20}$$

where S is an invariant measure of the strain rate and F_2 is a blending function which restricts the limiter to the wall boundary layer. Its formulation is based on the distance y to the nearest surface and on flow variables:

$$F_2 = tanh\big(arg_2^2\big) \tag{B.21}$$

with:

$$arg_2 = max\Big(\frac{2\sqrt{k}}{\beta'\omega y}, \frac{500\,\nu}{y^2\,\omega}\Big) \tag{B.22}$$